JGR Oceans

RESEARCH ARTICLE
10.1029/2018JC014716

Radiocarbon and Helium Isotope Constraints on Deep Ocean Ventilation and Mantle-^{3}He Sources

Tim DeVries[1,2] **and Mark Holzer**[3]

[1]Department of Geography, University of California, Santa Barbara, CA, USA, [2]Earth Research Institute, University of California, Santa Barbara, CA, USA, [3]School of Mathematics and Statistics, University of New South Wales, Sydney, New South Wales, Australia

Key Points:
- Radiocarbon and helium isotope measurements provide complementary constraints on the deep ocean ventilation in a circulation inverse model
- The assimilated circulation produces realistic westward propagating ^{3}He plumes in the deep Eastern Tropical Pacific
- The jointly assimilated globally integrated mantle-^{3}He source is 585–672 mol/year

Correspondence to:
T. DeVries,
tdevries@geog.ucsb.edu

Citation:
DeVries, T., & Holzer, M. (2019). Radiocarbon and helium isotope constraints on deep ocean ventilation and mantle-^{3}He sources. *Journal of Geophysical Research: Oceans*, *124*. https://doi.org/10.1029/2018JC014716

Received 29 OCT 2018
Accepted 12 APR 2019
Accepted article online 22 APR 2019

Abstract Radiocarbon (Δ^{14}C) and helium isotopes (δ^3He) have long been used to constrain the ocean's ventilation rates and to trace regional deep ocean circulation pathways, but they have not been fully exploited together to constrain the deep circulation in global models. Here we assimilate Δ^{14}C and δ^3He measurements into a global ocean circulation inverse model (OCIM) to jointly constrain the deep ocean circulation and the rate of mantle-helium injection at seafloor spreading ridges. We find that the new version of the inverse model (OCIM2) matches the observed Δ^{14}C and δ^3He distributions much better than a previous version (OCIM1) that assimilated objectively mapped Δ^{14}C but not δ^3He. OCIM2 features faster-ventilated bottom waters and slower-ventilated intermediate-depth waters in the Pacific and Indian Oceans. The mean time since *last* ventilation (ideal mean age) in Pacific bottom waters is up to 150 years younger, while middepth Pacific waters are up to several hundred years older. The δ^3He constraints are shown to be important for estimates of the mean time to *next* ventilation in the Pacific Ocean. The δ^3He constraints also favor jet-like currents in the deep equatorial Pacific to capture realistic westward propagating helium plumes emanating from the East Pacific Rise. The globally integrated mantle-helium source is 585–672 mol/year, compared to 400–1,000 mol/year from previous estimates. The major regional difference occurs in the Southern Ocean, where the OCIM2 mantle-helium source is up to threefold smaller than estimates based on ridge spreading rates.

1. Introduction

The ocean's deep circulation is difficult to observe directly, but observations of physical and chemical seawater properties can be used to reconstruct the rates and patterns of deep ocean circulation (e.g., Kawabe & Fujio, 2010; Lumpkin & Speer, 2007; Munk, 1966; Reid, 1997). The distributions of radiocarbon and helium isotopes are particularly well adapted for this purpose. Radiocarbon (^{14}C) is produced in the atmosphere by cosmic rays and enters the ocean via air-sea gas exchange. In the ocean interior ^{14}C decays with a half-life of 5,730 years (Godwin, 1962), which is longer than ocean mixing time scales, making ^{14}C a good constraint on deep ocean ventilation rates. Another useful property for constraining the deep ocean circulation is the ^{3}He/^{4}He stable-isotope ratio. In contrast to ^{14}C, which enters through the sea surface, helium is also dissolved in hydrothermal fluids vented along mid-ocean ridges. These fluids have a higher ^{3}He/^{4}He ratio than the atmosphere, and this elevated ^{3}He/^{4}He ratio provides a long-lived signature of transport pathways away from vent locations.

Radiocarbon has a long history of use as a tracer of deep ocean ventilation, both for the modern ocean and for past ocean states. Early box models and 1-D diffusion models used ^{14}C observations to constrain mixing rates between the surface and deep ocean (e.g., Broecker et al., 1960; Craig, 1969; Oeschger et al., 1975). More recently, radiocarbon observations have been used to infer the ventilation age of deep waters using inverse models (Gebbie & Huybers, 2012; Khatiwala et al., 2012) and tracer-only inversions (Holzer et al., 2010, 2018) and to constrain rates of ocean circulation and ventilation in global ocean inverse models (DeVries & Primeau, 2011; Schlitzer, 2007). Measurements of the Δ^{14}C of fossil foraminifera have also been used to constrain the circulation of the ocean during the last glacial maximum (Skinner et al., 2017) and the most recent deglaciation (Tschumi et al., 2010). (The abundance of ^{14}C is usually expressed relative to the abundance of the more common ^{12}C isotope and in turn normalized to the isotope ratio of the preindustrial atmosphere and corrected for biological fractionation effects. Using "delta" notation, a Δ^{14}C value (usually expressed in

units of ‰) greater than 0 indicates a $^{14}C/^{12}C$ ratio greater than that of the preindustrial atmosphere, while a value less than 0 indicates a $^{14}C/^{12}C$ ratio less than that of the preindustrial atmosphere.)

Numerous studies have also exploited the stable helium isotopes ^3He and ^4He to trace deep ocean circulation pathways. (δ^3He is defined analogously to $\Delta^{14}C$—where the measured $^3He/^4He$ ratio is normalized to the atmospheric $^3He/^4He$ ratio—and is usually expressed in units of percent. Note that δ^3He is not normalized for biological fractionation because there is no biological usage of helium). Lupton and Craig (1981) were the first to measure a plume of elevated δ^3He extending more than 2,000 km westward of the East Pacific Rise (EPR) in the southeast Pacific Ocean, indicating strong westward abyssal flows in this region. Stommel (1982) hypothesized that this feature was dynamically driven by buoyancy forcing from geothermal heating at the EPR hydrothermal vents. Subsequent inversions of hydrographic data supported the idea of a hydrothermally driven circulation in the deep southeast Pacific (Hautala & Riser, 1993). Prominent hydrothermal helium plumes have also been identified in the northeast Pacific (Lupton, 1998), southwest Pacific (Lupton et al., 2004), Indian Ocean (Srinivasan et al., 2004), Southern Ocean (Well et al., 2003), and Atlantic Ocean (Jenkins et al., 2015). These observations have been used to infer circulation patterns of the deep Indian Ocean (Srinivasan et al., 2004), to trace the pathway of bottom waters in the southwest Pacific (Downes et al., 2012), and to constrain diapycnal mixing rates in the Southern Ocean (Garabato et al., 2007).

Many dynamical global ocean circulation models have compared simulated radiocarbon and helium isotope ratios to observations in order to identify deficiencies in the simulated transport and to better understand controls on the deep ocean circulation. As part of the Ocean Carbon Cycle Model Intercomparison Project Phase 2 (OCMIP2), Matsumoto et al. (2004) compared simulated radiocarbon fields from 19 different global ocean circulation models and found that only about one fourth of them produced radiocarbon distributions in accord with observations. Also, as part of OCMIP2, Dutay et al. (2004) compared simulated and observed helium isotope ratios for six global ocean circulation models and found that none of the models correctly captured the extent of the observed helium plumes in the deep ocean. Other process-based modeling studies have shown that modeled deep ocean helium and radiocarbon distributions are sensitive to the representation of diapycnal and isopycnal mixing (Bardin et al., 2014; Dutay et al., 2010; Gnanadesikan et al., 2004) and to the inclusion of geothermal heating (Dutay et al., 2010; Gnanadesikan et al., 2015).

Despite the established utility of radiocarbon and helium isotopes as circulation and ventilation tracers, they have not been used together to constrain the deep circulation in global ocean models. Several global ocean circulation models have assimilated radiocarbon data to constrain their deep ocean circulation fields (DeVries & Primeau, 2011; DeVries, 2014; Schlitzer, 2007), and two of these models have been used to simulate helium isotope distributions and to infer mantle-^3He sources (Holzer et al., 2017; Schlitzer, 2016). Although these inverse models generally show a much better agreement with the observed ^3He distribution than dynamical (forward) ocean models, even these inverse models do not correctly capture the propagation of δ^3He plumes in the deep ocean. This indicates that the distributions of δ^3He contains important information about the deep circulation that is not captured by radiocarbon and the other tracers that were also assimilated by these inverse models. Furthermore, these inverse models relied on objectively mapped climatologies of $\Delta^{14}C$ from the Global Ocean Data Analysis Project (GLODAP; Key et al., 2004), which have significant errors due to attempts to correct for the influence of radiocarbon produced during nuclear bomb testing in the 1950s and 1960s (Key et al., 2004). These errors propagate into the resulting circulation estimates, biasing the inferred deep ocean circulation and ventilation rates.

Here, we use global data sets of $\Delta^{14}C$ and δ^3He measurements to constrain the large-scale global deep ocean circulation. We build upon a previous global OCIM that is constrained by observations of potential temperature, salinity, CFC-11, and GLODAP $\Delta^{14}C$ (DeVries, 2014). Instead of using the GLODAP $\Delta^{14}C$, here we assimilate raw $\Delta^{14}C$ data, along with a global data set of δ^3He observations, to jointly optimize the hydrothermal ^3He sources and the deep ocean circulation (section 2). We compare simulated $\Delta^{14}C$ and δ^3He fields to observations and to results from the previous version of the OCIM (sections 3.1 and 3.2). We quantify the influence of assimilating the raw $\Delta^{14}C$ and δ^3He observations on metrics of the deep ventilation (section 3.3) and on the large-scale overturning and lateral circulations of the deep ocean (section 3.4). We examine the inferred optimal mantle-^3He source distribution and discuss its implications for hydrothermal sources of trace metals (section 3.5). We discuss remaining uncertainties in section 4 and conclude in section 5.

2. Methods

We use an adjoint method (Thacker & Long, 1988) to jointly optimize a linearized dynamical circulation model and the sources and sinks of passive tracers. The approach used here is similar to that of DeVries and Primeau (2011), who first used the method to estimate the climatological steady state ocean circulation at 4° resolution using potential temperature, salinity, and GLODAP Δ^{14}C as tracer constraints. That work was updated and improved by DeVries (2014), who increased the resolution of the model to 2° in the horizontal, added CFC-11 as an additional tracer constraint, and improved the numerics and subgrid-scale mixing parameterizations. The model described by DeVries (2014) is referred to as the ocean circulation inverse model (OCIM). In this study, we replace the GLODAP Δ^{14}C with bomb-screened raw Δ^{14}C data, and we additionally assimilate bomb-screened δ^3He data. To distinguish the new and old versions of the OCIM, we call the previous version OCIM1 (DeVries, 2014) and the version described here OCIM2.

The remainder of this section provides a brief overview of the OCIM methodology and a description of the new observational constraints used in this study.

2.1. Ocean Circulation Model and Tracer Transport Model

The ocean circulation model obeys linearized Navier-Stokes equations, which can be written in matrix form as

$$\frac{\mathrm{d}\mathbf{x}}{\mathrm{d}t} + \mathbf{M}\mathbf{x} = \mathbf{d} + \mathbf{e}, \tag{1}$$

where the vector $\mathbf{x}$ organizes the dynamical variables, including the horizontal and vertical velocities and the sea surface height; $\mathbf{M}$ is a matrix containing the coefficients for the Coriolis and frictional forces, and the continuity constraints; $\mathbf{d}$ is a vector containing the wind stress and baroclinic pressure gradient forces diagnosed from the observed climatological density field; and $\mathbf{e}$ is an adjustable model error term to account for inaccuracies in $\mathbf{d}$ and $\mathbf{M}$ (e.g., discretization errors and neglected nonlinear terms). Equation (1) is discretized on an Arakawa B grid (Arakawa & Lamb, 1977) at 2° horizontal resolution with 24 vertical levels and solved at steady state ($\mathrm{d}\mathbf{x}/\mathrm{d}t = 0$). Additional discussion and details on the model formulation is provided by DeVries and Primeau (2011) and DeVries (2014).

For a given error vector $\mathbf{e}$, we solve equation (1) to obtain the dynamical state $\mathbf{x}$ of the model. We then use the modeled horizontal and vertical velocities, along with imposed isopycnal ($\kappa_{\|}$) and diapycnal ($\kappa_{\perp}$) diffusivities, to construct a discretized transport operator matrix $\mathbf{T}$. Isopycnal diffusion acts along isopycnals determined from observed annual mean climatological temperature and salinity distributions and truncated at a maximum slope of 10^{-2} m/m, allowing application of the small-slope approximation of the Redi diffusion tensor (Griffies et al., 1998). Diapycnal diffusion is approximated as acting vertically. Both $\kappa_{\|}$ and $\kappa_{\perp}$ are prescribed as globally uniform and held constant.

The transport operator $\mathbf{T}$ is used to calculate the evolution of the tracers by solving

$$\frac{\mathrm{d}\mathbf{c}}{\mathrm{d}t} + \mathbf{T}(\mathbf{x}(\mathbf{e}), \kappa_{\|}, \kappa_{\perp})\mathbf{c} = \mathbf{q}(\mathbf{c}), \tag{2}$$

where $\mathbf{c}$ is the tracer concentration and $\mathbf{q}(\mathbf{c})$ is the vector of the corresponding tracer sources and sinks. We simulate six tracers: potential temperature (θ), salinity (S), radiocarbon (which is modeled as the normalized $^{14}C/^{12}C$ ratio), CFC-11, and the helium isotopes ^{3}He and ^{4}He.

All tracers have sources and sinks at the sea surface due to air-sea exchange. For θ and S, this is modeled by restoring to an adjustable surface-ocean field with a 30-day restoring time scale, as described in DeVries and Primeau (2011). The air-sea exchange of CFC-11, helium isotopes, and radiocarbon depends on their saturation concentration ($\mathbf{c}_{\mathrm{sat}}$) and a wind speed-dependent piston velocity (k), following

$$\mathbf{q}_{\text{air-sea}} = \frac{k}{\Delta z_1}(\mathbf{c}_{\mathrm{sat}} - \mathbf{c}), \tag{3}$$

where Δz_1 is the depth of the model's surface layer. The saturation concentration for CFC-11 is determined from its temperature- and salinity-dependent solubility (Warner & Weiss, 1985) and the atmospheric CFC-11 history (Bullister, 2015). The saturation concentration for ^{4}He is determined from its temperature- and

salinity-dependent solubility (Weiss, 1971), and the saturation concentration of ^{3}He is determined by reducing the solubility by a factor of 0.984 relative to that of ^{4}He (Top et al., 1987) and taking into account the relative abundance of ^{3}He:^{4}He in the atmosphere, $R^{^3He}_{atm}$, which is set to 1.384×10^{-6} following previous studies (e.g., Holzer et al., 2017). The saturation concentration of radiocarbon is set to 1, to represent the normalized $^{14}C/^{12}C$ ratio in the preindustrial atmosphere. The piston velocity k is parameterized as a quadratic function of wind speed (e.g., Wanninkhof, 1992):

$$k = \gamma \langle u_{10} \rangle^2 (Sc/660^{-1/2})(1 - f_{ice}), \tag{4}$$

where $\langle u_{10} \rangle$ is the root-mean-square wind speed at 10 m above the sea surface, Sc is the Schmidt number, and f_{ice} is the climatological ice fraction cover. $\langle u_{10} \rangle$ and f_{ice} are averages of 6-hr wind speed and daily sea ice fraction from the National Centers for Environmental Prediction reanalysis data for the period 1948–2016 (Kalnay et al., 1996). The coefficient γ, which is allowed to vary with position, controls the piston velocity and is determined as part of the solution of the inverse model (see section 2.2). For radiocarbon, we adjusted γ to account for the ratio of CO_2 to dissolved inorganic carbon (DIC) following the formulation by DeVries and Primeau (2010). For this, we used the CO_2 concentration in equilibrium with preindustrial atmospheric pCO_2 of 280 μatm, and the preindustrial DIC concentration from GLODAP (Key et al., 2004). This formulation for the air-sea transfer of radiocarbon gives results nearly identical to those from using an abiotic model that separately solves for the air-sea flux of ^{12}C and ^{14}C, as in the Ocean Model Intercomparison Project protocol (Orr et al., 2017).

In addition to sources and sinks at the sea surface, radiocarbon also has a sink from radioactive decay, and ^{3}He and ^{4}He have sources from hydrothermal vents. Hydrothermal vents are located along spreading ocean ridges at the same locations as in OCMIP2 (Dutay et al., 2004). However, while the OCMIP2 models specify mantle helium injection rates as proportional to ridge spreading rates, here we allow the local rate of mantle helium injection to be an adjustable parameter that is determined as part of the solution to the inverse model. Mantle helium is assumed to be eightfold enriched in ^{3}He relative to atmospheric helium, following previous modeling studies (e.g., Dutay et al., 2004; Holzer et al., 2017).

2.2. Inversion Procedure and Observational Constraints

Solutions to model equations (1) and (2) can be determined for a given set of "control" parameters $\mathbf{p}$. The set of control parameters includes the errors terms $\mathbf{e}$ in the dynamical equations; surface restoring fields for temperature and salinity; the gas exchange coefficient γ; and the local mantle-^{3}He injection rate along spreading ridges.

The inverse model determines the "optimal" set of parameters $\hat{\mathbf{p}}$ by minimizing a quadratic cost function,

$$J(\mathbf{p}) = [\mathbf{y}(p) - \mathbf{y}^{obs}]^T \Gamma_{yy}^{-1} [\mathbf{y}(p) - \mathbf{y}^{obs}] + \frac{1}{\omega^2} (\mathbf{p} - \mathbf{p}_0)^T \Gamma_{pp}^{-1} (\mathbf{p} - \mathbf{p}_0), \tag{5}$$

where $\mathbf{y}(p)$ is a vector of model state variables including the dynamical variables $\mathbf{x}$, the tracer concentrations $\mathbf{c}$, and surface heat and salt fluxes from the surface restoring; $\mathbf{y}^{obs}$ is a vector of corresponding observations; Γ_{yy} is the covariance matrix for the observations; ω is a hyperparameter controlling the relative weights of the state variables and control parameters in the cost function and is set to $\omega = 3$ following DeVries (2014); $\mathbf{p}_0$ is the initial guess at the control parameters; and Γ_{pp} is the prescribed covariance matrix for the control parameters.

The terms of equation (5) are formulated as described by DeVries and Primeau (2011) and updated by DeVries (2014), and the reader is referred to these publications for more details on the formulation of the cost function. The key modifications to the cost function made in this study are as follows:

1. The vector of observations $\mathbf{y}^{obs}$ was modified by adding δ^3He data and by replacing the GLODAP Δ^{14}C data with raw (unmodified) Δ^{14}C data screened for contamination by bomb-produced radiocarbon (see section 2.3).
2. The covariance matrix for the observations Γ_{yy} was modified to account for the variance of the Δ^{14}C and δ^3He observations on the model grid.
3. Γ_{yy} was further modified to increase the penalty applied to vertical velocities fiftyfold compared to the penalty used by DeVries (2014). This was necessary in order to achieve vertical velocities similar to those

recently estimated from the Estimating the Circulation and Climate of the Ocean data assimilation, which employs full dynamics (Liang et al., 2017).

4. The vector of control parameters $\mathbf{p}$ was expanded to include the local mantle-^{3}He injection rates along ocean ridges. No prior constraints were applied to the mantle-^{3}He source, that is, $\Gamma_{pp}^{-1} = 0$ for the mantle helium sources.
5. The prior value for the gas exchange piston velocity parameter γ in the vector $\mathbf{p}_0$ was set to 0.251 cm·hr^{-1}·m^2·s^{-2} following the most recent estimates (Wanninkhof et al., 2013). This contrasts with the prior value of $\gamma = 0.334$ cm·hr^{-1}·m^2·s^{-2} used in OCIM1.

The treatment of the Δ^{14}C and δ^3He observations is described in the following subsection.

2.3. Δ^{14}C and δ^3He Observations

While DeVries (2014) used objectively mapped GLODAP Δ^{14}C concentrations (Key et al., 2004), here we use raw Δ^{14}C observations from GLODAPv2 (Olsen et al., 2016). Because we do not model the bomb Δ^{14}C transient, we screened the raw Δ^{14}C observations for potential contamination by bomb Δ^{14}C. We first excluded all Δ^{14}C observations above 1,500-m depth as potentially contaminated by bomb radiocarbon. In addition, we eliminated observations at all depths north of the equator in the Atlantic, and south of 35°S in the Southern Ocean, because these regions contain deep waters that are likely to contain bomb radiocarbon. Exceptions to these exclusions were allowed if a given Δ^{14}C measurement was paired with a near-zero CFC-11 or CFC-12 measurement (CFC-11 < 0.05 pmol/kg or CFC-12 < 0.025 pmol/kg). We supplemented the GLODAPv2 Δ^{14}C data set with a compilation of Δ^{14}C measurements from surface corals (Guilderson et al., 2005), historical ocean cruises compiled by Graven et al. (2012), and a collection of prebomb surface-ocean radiocarbon ages from the 14CHRONO Marine Reservoir Database available at the website (http://calib.org/marine/). The coral and 14CHRONO data record the Δ^{14}C of skeletal remains of marine organisms, rather than the actual seawater Δ^{14}C. For these data, we only included samples whose formation is estimated to have occurred prior to 1955 (determined from the samples' "calendar age").

The δ^3He data were also taken from the GLODAPv2 compilation (Olsen et al., 2016), with additional data from a transect in the eastern Pacific at roughly 12°S (Jenkins et al., 2017). Like radiocarbon, δ^3He has a source from nuclear weapons testing, which produced tritium (^{3}H) that decays to ^{3}He. Because we do not model this source of ^{3}He, we removed δ^3He observations that might include tritiugenic ^{3}He. Like for our treatment of Δ^{14}C, we removed data above 1,500 m in all ocean basins and all data north of the equator in the Atlantic. Unlike for Δ^{14}C, however, we did not remove δ^3He measurements below 1,500 m in the Southern Ocean, because the source of tritium to the ocean was concentrated in the Northern Hemisphere where most nuclear weapons testing took place (Stark et al., 2004). Exceptions to these restrictions are allowed if a given δ^3He measurement is paired with a near-zero CFC-11 or CFC-12 measurement (CFC-11 < 0.05 pmol/kg or CFC-12 < 0.025 pmol/kg).

All Δ^{14}C and δ^3He observations were binned to the model grid by averaging all observations within a given grid cell. The variance of Δ^{14}C and δ^3He at model grid points containing observations was computed from the stated uncertainty of the original data sources, assuming independence of errors. After computing the uncertainty of observations on the model grid, we set a minimum uncertainty of 4‰ and 0.5% for Δ^{14}C and δ^3He, respectively, based on the interannual variation of observations from repeat transects. Grid points without any observations were assigned an extremely high uncertainty so as to give them negligible weight in the cost function. The estimated variance at each grid point was placed along the diagonal of Γ_{yy}, and a discretized Laplacian operator was added to Γ_{yy} to penalize grid-scale noise in the simulated Δ^{14}C and δ^3He fields. The "noisiness" penalties are generally an order of magnitude smaller than the penalties for misfit with the observations.

2.4. Optimization and Sensitivity Analysis

The optimal parameter set $\hat{\mathbf{p}}$ was determined by minimizing equation (5) using a quasi-Newton algorithm called the limited-memory Broyden-Fletcher-Goldfarb-Schano method (Nocedal & Wright, 2006). This search method does not guarantee convergence to a global minimum, so it is possible that only one of the potentially multiple minima is found. The optimization is terminated when the value of the cost function changes by less than 1% per 1,000 iterations (Schlitzer, 2007). This occurs after about 5,000-10,000 iterations.

We performed two optimizations. In the first optimization, we jointly optimized parameters controlling the circulation and air-sea gas exchange using potential temperature, salinity, radiocarbon, and CFC-11 (i.e.,

Table 1
The Mean Deviation (MD), Root-Mean-Square Error (RMSE) and Relative Error (RE) of Tracer Fields for Each of the Model Configurations

Model	Metric	Temperature (°C)	Salinity (psu)	Δ^{14}C (‰)	CFC-11 (pmol/kg)	δ^3He (%)
CTL	MD	−0.04	−0.00	−0.07	−0.04	−0.02
$\kappa_{\|\|} = 1,000$ m^2/s	RMSE	0.41	0.075	6.0	0.26	0.72
$\kappa_{\perp} = 10^{-5}$ m^2/s	RE	1.21	0.83	2.08	2.46	1.61
LOW-ISO	MD	−0.04	−0.00	−0.07	−0.04	−0.01
$\kappa_{\|\|} = 600$ m^2/s	RMSE	0.43	0.074	5.3	0.26	0.60
$\kappa_{\perp} = 10^{-5}$ m^2/s	RE	1.16	0.81	1.76	2.27	1.18
HIGH-ISO	MD	−0.04	0.00	−0.08	−0.04	−0.03
$\kappa_{\|\|} = 2,000$ m^2/s	RMSE	0.42	0.078	7.3	0.27	0.91
$\kappa_{\perp} = 10^{-5}$ m^2/s	RE	1.55	1.06	2.87	3.10	2.64
HIGH-DIA	MD	−0.05	0.00	0.15	−0.04	−0.02
$\kappa_{\|\|} = 1,000$ m^2/s	RMSE	0.41	0.074	7.7	0.27	0.83
$\kappa_{\perp}$ up to 3×10^{-4} m^2/s	RE	1.51	0.94	3.28	2.57	2.17
HIGH-DIA+LOW-ISO	MD	−0.05	0.00	0.10	−0.05	−0.01
$\kappa_{\|\|} = 600$ m^2/s	RMSE	0.42	0.074	6.7	0.27	0.70
$\kappa_{\perp}$ up to 3×10^{-4} m^2/s	RE	1.34	0.87	2.58	2.37	1.58
HIGH-DIA+HIGH-ISO	MD	−0.05	0.00	0.18	−0.04	−0.04
$\kappa_{\|\|} = 2,000$ m^2/s	RMSE	0.43	0.081	9.6	0.28	1.04
$\kappa_{\perp}$ up to 3×10^{-4} m^2/s	RE	2.10	1.25	5.14	3.04	3.41

Note. The RE is unitless. See text for details.

δ^3He was not included as a constraint). In the second optimization, we included δ^3He and jointly optimized parameters controlling the circulation and mantle-^{3}He sources. This separation was done for two reasons. First, the impact of δ^3He constraints on the deep ocean circulation and ventilation can be diagnosed from the difference between the two optimizations. Second, because the δ^3He is affected in opposite ways by gas exchange (which introduces isotopically light helium into the ocean) and mantle helium sources (which introduce isotopically heavy helium into the ocean), it may be difficult to disentangle these processes using δ^3He data, especially in locations where surface and bottom waters rapidly mix, for example, in the Southern Ocean. Therefore, for the second optimization, the air-sea gas exchange parameter (γ) was held constant at the value determined in the first optimization.

We also investigated the sensitivity of the optimal solution to the value of the isopycnal diffusivity $\kappa_{||}$ and diapycnal diffusivity $\kappa_{\perp}$ in the transport operator. We focus on these parameters because previous studies have shown that modeled δ^3He distributions and inferred mantle-^{3}He sources are sensitive to the values of subgrid-scale diffusivities (Dutay et al., 2010; Holzer et al., 2017). In the control simulation (CTL) we used a uniform value of $\kappa_{||} = 1,000$ m^2/s everywhere and a small background value of $\kappa_{\perp} = 10^{-5}$ m^2/s outside the surface mixed layer. (The same values of $\kappa_{||}$ and $\kappa_{\perp}$ were used in the control simulation of OCIM1 (DeVries, 2014). One set of sensitivity simulations maintains the CTL model's low background value of $\kappa_{\perp}$ outside the surface mixed layer but varies $\kappa_{||}$ from 600 m^2/s (LOW-ISO) to 2,000 m^2/s (HIGH-ISO). Another set of sensitivity simulations increases $\kappa_{\perp}$ with depth using the formulation of Tsujino et al. (2000; their Type-II profile), in which $\kappa_{\perp}$ increases from 10^{-5} m^2/s at the surface to 3×10^{-4} m^2/s at 5400 m. These HIGH-DIA simulations were repeated using the same three combinations of $\kappa_{||}$ as used for the low-diapycnal diffusivity models. Table 1 summarizes the diffusivity combinations investigated here.

3. Results and Discussion

After optimization, the simulated and observed tracer distributions are in good agreement, as demonstrated by the model statistics (Table 1; reported statistics shown in Table 1 are for the optimization that includes

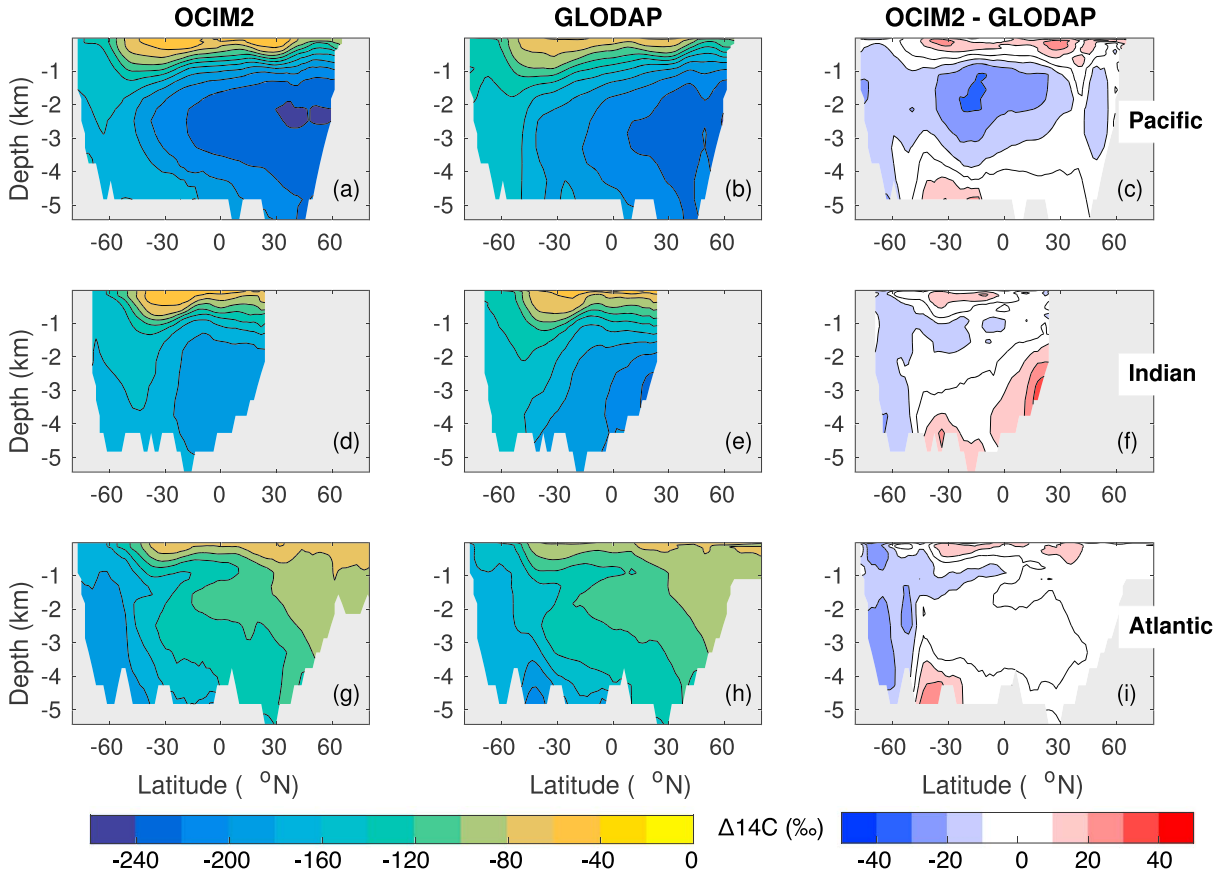

Figure 1. Zonally basin-averaged prebomb ("natural") $\Delta^{14}C$ simulated by OCIM2 (a, d, and g) compared to GLODAP-mapped natural $\Delta^{14}C$ (b, e, and h), and the difference between OCIM2 and GLODAP $\Delta^{14}C$ (c, f, and i) in the Pacific (a–c), Indian (d–f), and Atlantic (g–i) Oceans. GLODAP = Global Ocean Data Analysis Project; OCIM = ocean circulation inverse model.

the δ^3He constraint.) Table 1 reports the (volume-weighted) mean difference (MD) between the model state and the observations, and the (volume-weighted) root mean square deviation (RMSE) between the model state and the observations. Also shown is the relative error (RE), which measures the magnitude of the model-data misfit relative to that expected due to observational uncertainties. The MD and RMSE are very close to their values in the OCIM1 model (DeVries, 2014, their Table 2), although the RMSE for temperature, salinity, and CFC-11 are slightly higher for OCIM2 than for OCIM1.

The different sensitivity versions of OCIM2 vary most in terms of their fit to $\Delta^{14}C$ and δ^3He. The RE for δ^3He varies from 1.18 in the LOW-ISO model to 3.41 in the HIGH-DIA+HIGH-ISO model. The RE for $\Delta^{14}C$ is also lowest in the LOW-ISO model ($RE = 1.76$) and highest in the HIGH-DIA+HIGH-ISO model ($RE = 5.14$). In general, the models with higher diffusivities have poorer fits to the observations (Table 1). Much of this may be explained by the fact that higher-diffusivity models have smoother tracer fields, which are less able to capture small-scale features of the tracer distributions. Some of these small-scale features may result from only a few measurements and may not be representative of the climatological average, and thus, the higher-diffusivity models may not necessarily be "worse" than the others; indeed, the less smooth models might to some degree be overfitting undersampled observations. Nonetheless, the highest-diffusivity case (HIGH-DIA+HIGH-ISO) is so poor compared to the other models that we eliminate this model from consideration.

In the following, we will plot results from the CTL model unless otherwise noted. We choose this as the standard simulation for consistency with DeVries (2014), but we consider the results from the other models (with the exception of HIGH-DIA+HIGH-ISO) as equally valid in most respects. Where uncertainties are given, they represent the half-range of the first five models listed in Table 1 (i.e., without including the HIGH-DIA+HIGH-ISO case).

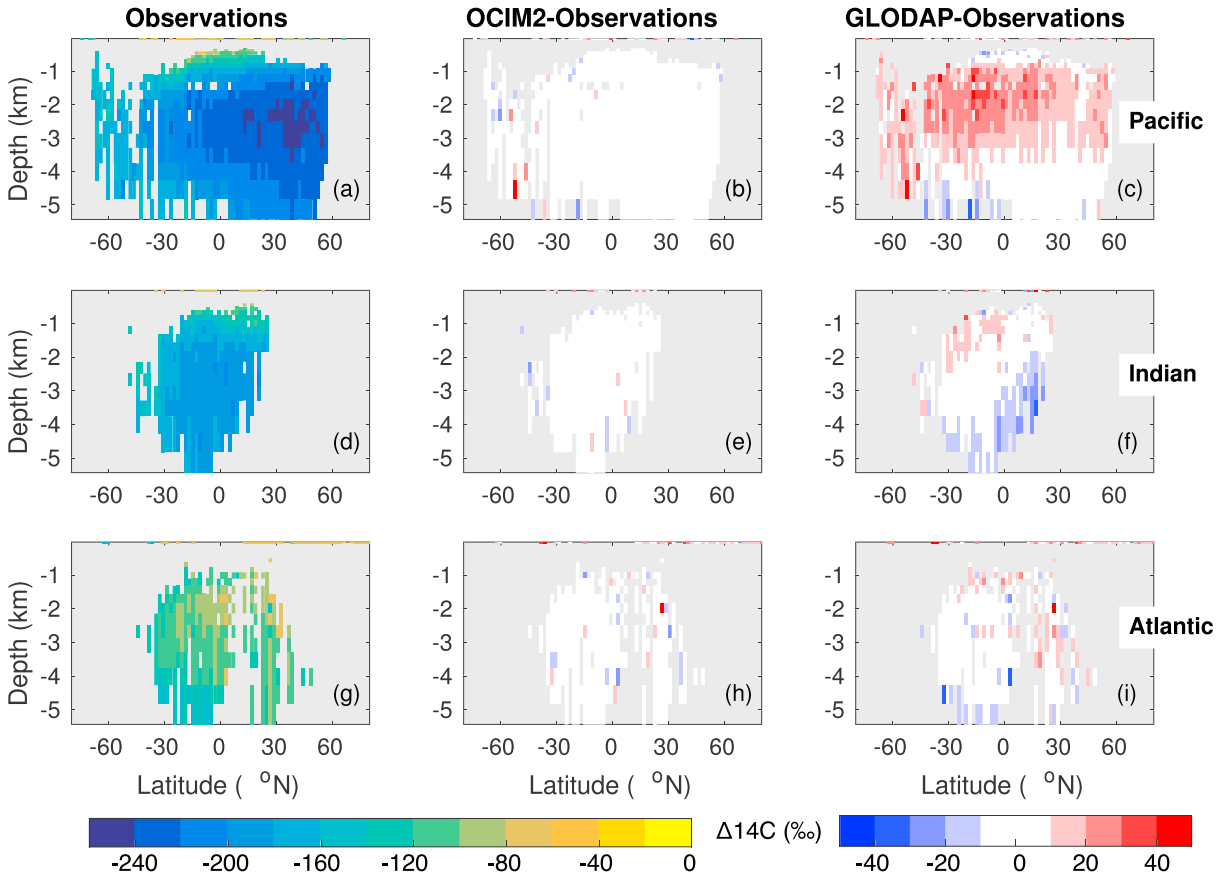

Figure 2. Zonally basin-averaged observed prebomb ("natural") $\Delta^{14}C$ from our data compilation (a, d, and g), the difference between the OCIM2-simulated and observed natural $\Delta^{14}C$ (b, e, and h), and between GLODAP and observed natural $\Delta^{14}C$ (c, f, and i) in the Pacific (a–c), Indian (d–f), and Atlantic (g–i) Oceans. GLODAP = Global Ocean Data Analysis Project; OCIM = ocean circulation inverse model.

3.1. Simulated Natural $\Delta^{14}C$ and Comparison With Observations and GLODAP

The optimal $\Delta^{14}C$ distribution in OCIM2 shows the aging of deep ocean waters from the North Atlantic, where $\Delta^{14}C$ values are roughly −80‰, into the North Pacific where $\Delta^{14}C$ values reach a minimum of −240‰ at depths of ~2,000 m (Figure 1). The OCIM2 $\Delta^{14}C$ distribution shows some clear differences with the GLODAP-mapped prebomb $\Delta^{14}C$ climatology. In the Pacific Ocean, the low $\Delta^{14}C$ values at middepths extend further into the South Pacific in the OCIM2 (Figure 1a) as compared to GLODAP (Figure 1b). The OCIM2 also predicts slightly higher values of $\Delta^{14}C$ in the deep South Pacific (Figure 1c). A similar pattern is found in the Indian Ocean, where the OCIM2 $\Delta^{14}C$ values are higher in the deep ocean and lower in intermediate waters than in the GLODAP climatology (Figure 1f). In the Atlantic Ocean, the major difference between OCIM2 and GLODAP $\Delta^{14}C$ is found in the Southern Ocean, where bottom waters north of 50°N have higher $\Delta^{14}C$ in OCIM2 compared to GLODAP, while Southern Ocean waters south of 50°N have lower $\Delta^{14}C$ in OCIM2 as compared to GLODAP (Figure 1i).

The OCIM2 $\Delta^{14}C$ field shows little difference compared to the observed $\Delta^{14}C$ data (Figure 2). The mismatch between OCIM2-simulated and observed $\Delta^{14}C$ is small with an RMSE of ~6‰ (Table 1), and the local differences are not coherent, with no discernable spatial pattern at the basin scale (Figures 2b, 2e, and 2h). On the other hand, the GLODAP-mapped $\Delta^{14}C$ shows coherent deviations from the observations, particularly in the Pacific Ocean where the middepth $\Delta^{14}C$ in GLODAP is 20–40‰ too high (Figure 2c), and bottom waters of the South Pacific and Indian Oceans where the GLODAP $\Delta^{14}C$ is 10–20‰ lower than observed (Figures 2c and 2f). GLODAP $\Delta^{14}C$ is also 10–20‰ too high in the Southern Ocean, at least in the Pacific sector where there are concurrent CFC measurements below the CFC detection limit, indicating that the $\Delta^{14}C$ measurements are representative of prebomb conditions (Figure 2c).

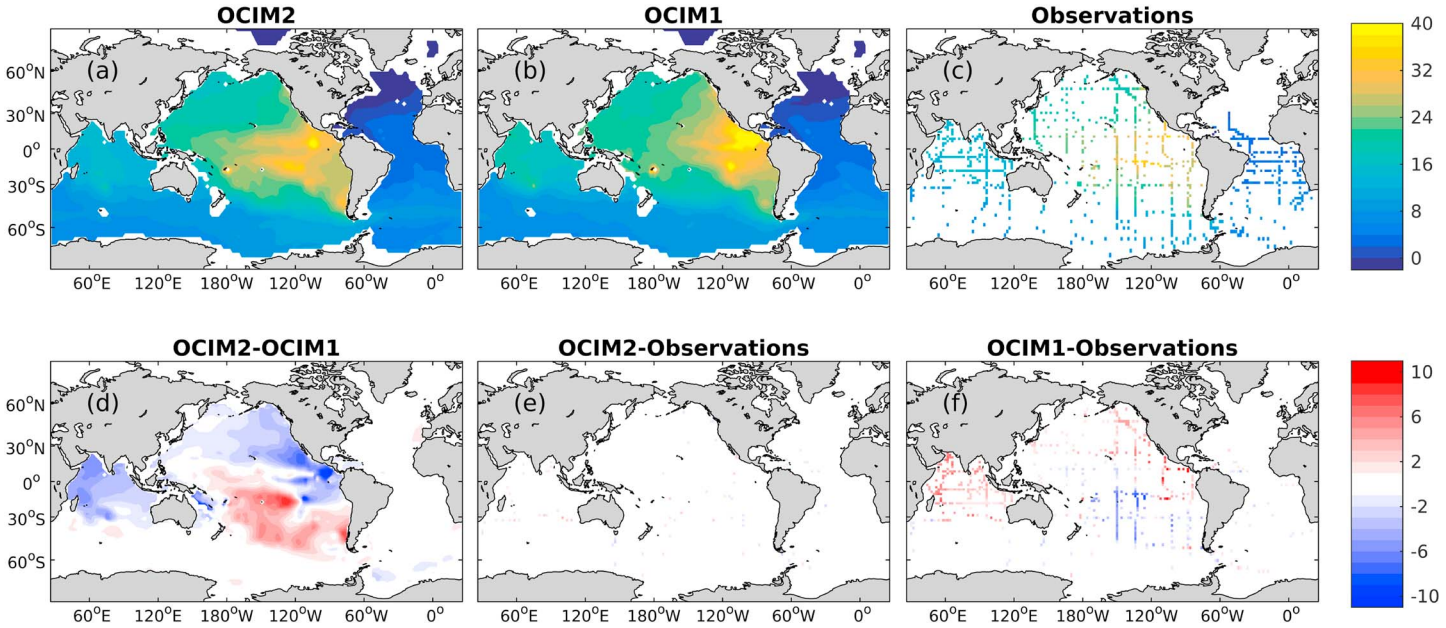

Figure 3. δ^3He distribution averaged over the depth interval 2,000–3,000 m as simulated by OCIM2 (a), OCIM1 (b), and from the observations (c). Also shown are the difference between OCIM2- and OCIM1-simulated δ^3He (d), the difference between OCIM2-simulated and observed δ^3He (e), and between OCIM1-simulated and observed δ^3He (f). Panels (a)–(c) have a contour interval of 2%. Panels (d)–(f) have a contour interval of 1%. For these calculations, both models used the same (optimized) mantle-^{3}He source distribution. OCIM = ocean circulation inverse model.

Overall, OCIM2 shows good fidelity to the observed Δ^{14}C without systematic errors. Compared to GLODAP, OCIM2 has a natural (prebomb) Δ^{14}C distribution that is lower in middepth waters and in the Southern Ocean, and higher in bottom waters, in better agreement with the observations. The OCIM2 Δ^{14}C distribution implies that middepth and Southern Ocean waters are more poorly ventilated (older radiocarbon ages) and that bottom waters are better ventilated (younger radiocarbon ages), than implied by the GLODAP product. Given OCIM2's improved fidelity to observations, we recommend the OCIM2 Δ^{14}C climatology as an alternative to the GLODAP prebomb Δ^{14}C product.

The Δ^{14}C distributions shown in Figures 1 and 2 are robust across the suite of sensitivity runs. Uncertainties in the modeled Δ^{14}C due to variations in the isopycnal and diapycnal diffusivity, defined as half the ensemble range, are ~1–2‰ over most of the ocean. In the Southern Ocean (<40°S) uncertainties are ~5‰, and the largest uncertainties of 5–10‰ occur in the intermediate and mode waters of the sub-Antarctic (20–40°S) and North Pacific (>30°N).

3.2. Simulated δ^3He Distribution and Large-Scale Hydrothermal Plumes

After jointly optimizing the local mantle-^{3}He injection rates and the ocean circulation, the OCIM2-simulated δ^3He distribution closely matches the observations. The global RMSE between OCIM2-simulated and observed δ^3He is 0.72% in the CTL simulation (Table 1). If the same (optimized) mantle-^{3}He sources are used to simulate δ^3He using the OCIM1 circulation, the model-data misfit is much larger with an RMSE of 3.7%. The differences between the OCIM2 and OCIM1-simulated δ^3He can be seen most clearly at 2,500-m depth, which is the approximate mean depth of mantle-^{3}He injection (Figure 3). OCIM1 δ^3He is too high in the Indian Ocean and northeast Pacific compared to both OCIM2 and the observations, while OCIM1 δ^3He is too low in the South Pacific.

Particularly prominent in OCIM2 are westward propagating δ^3He plumes emanating from the EPR to the north and south of the equator (Figure 3a). By contrast, the OCIM1 circulation produces δ^3He plumes that diffuse laterally in both directions away from the ridge sources, which is not observed (Figure 3b). The propagation of δ^3He plumes away from the EPR can be seen most clearly along a zonal transect in the southeast Pacific that was recently occupied by GEOTRACES cruise GP16 (Figures 4a and 4b; Jenkins et al., 2015). To match the observed westward propagating δ^3He plume in this region, OCIM2 predicts mean westward velocities of 0.7 $\pm$ 0.2 cm/s in the center of the plume (2,000- to 3,000-m depth, δ^3He > 30 %; error bars are ensemble half-range). By contrast, the corresponding westward velocity of OCIM1 is only 0.1 $\pm$ 0.3 cm/s.

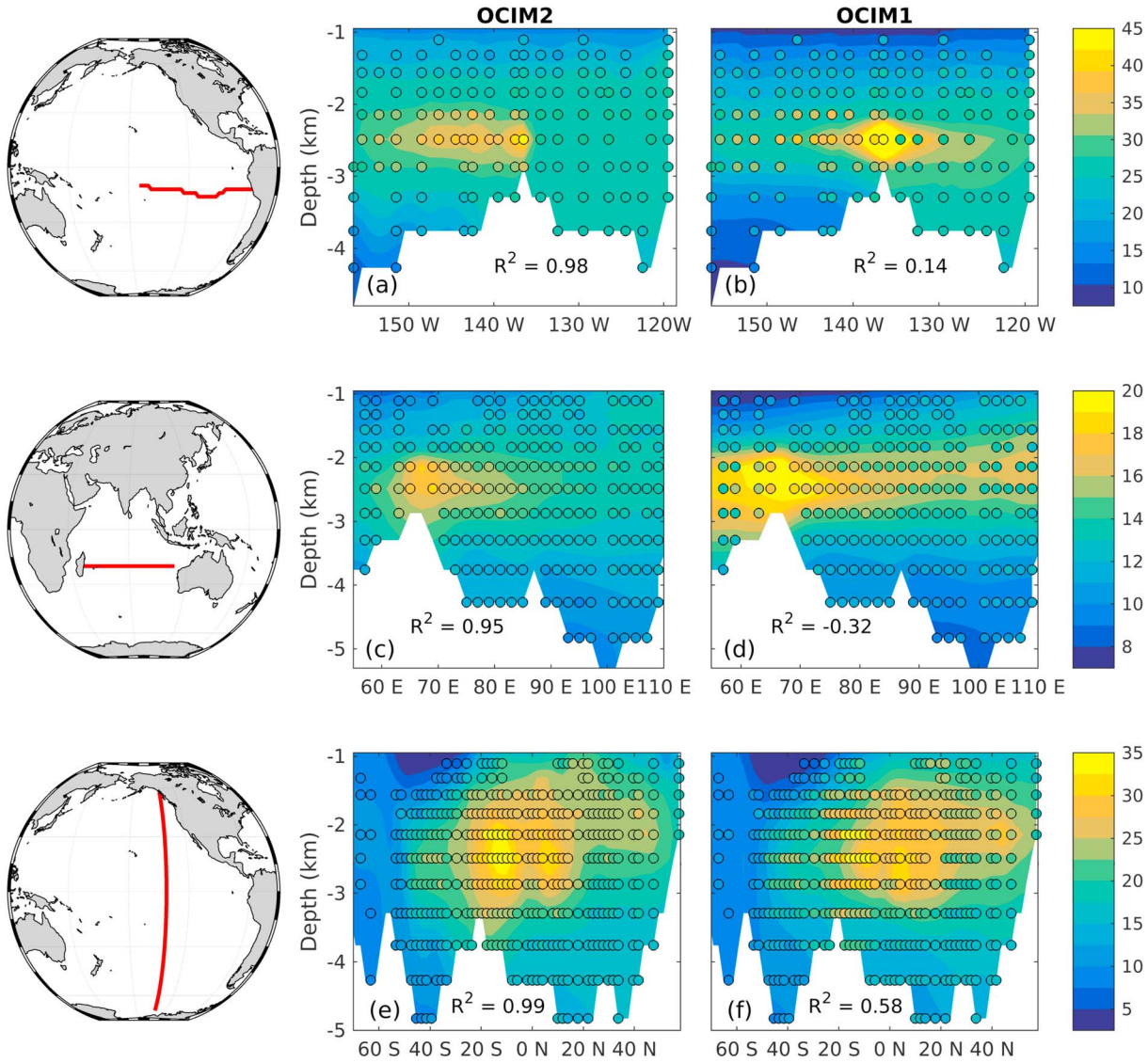

Figure 4. Observed (colored circles) and modeled (contoured) δ^3He along vertical cross sections for OCIM2 (a, c, and e) and for OCIM 1 (b, d, and f). Units are percent in all plots. R^2 values of the model fit to the observations are indicated at the bottom of the contoured sections. The maps show the geographic locations of the plotted cross sections. For these calculations, both models used the same (optimized) mantle-^{3}He source. OCIM = ocean circulation inverse model

Similar results are found for δ^3He plumes in other locations. For example, at 20°S in the Indian Ocean, an eastward propagating δ^3He plume is correctly captured by OCIM2 (Figure 4c), but OCIM1 lacks this feature and overpredicts δ^3He values at the depths of the observed plume (Figure 4d). A meridional transect along 135°W in the Pacific demonstrates that OCIM2 better captures the lateral extent of δ^3He plumes at 2,500-m depth emanating from roughly 15°S and 10°N, with lower δ^3He values along the equator (Figure 4e). However, even OCIM2 does not simulate sufficiently low δ^3He at the equator, perhaps indicating that eastward flow in the deep equatorial Pacific is too weak. This could be related to the coarse resolution of OCIM2, which cannot resolve equatorial currents very well. In the Southern Ocean, OCIM2 corrects a slight low bias in δ^3He that is present in OCIM1 (Figure 4f).

3.3. Ventilation of the Intermediate and Deep Ocean

Given the high fidelity of the OCIM2-simulated Δ^{14}C and δ^3He to the observations, OCIM2 can be used to derive reliable estimates of ocean ventilation times. Here we consider the mean time since last ventilation anywhere at the surface (often called the ideal mean age but also ventilation age or mean last-passage time) and the mean time to next ventilation at the surface (also called mean reexposure time or mean first-passage time (Primeau, 2005)). We begin with the ideal mean age.

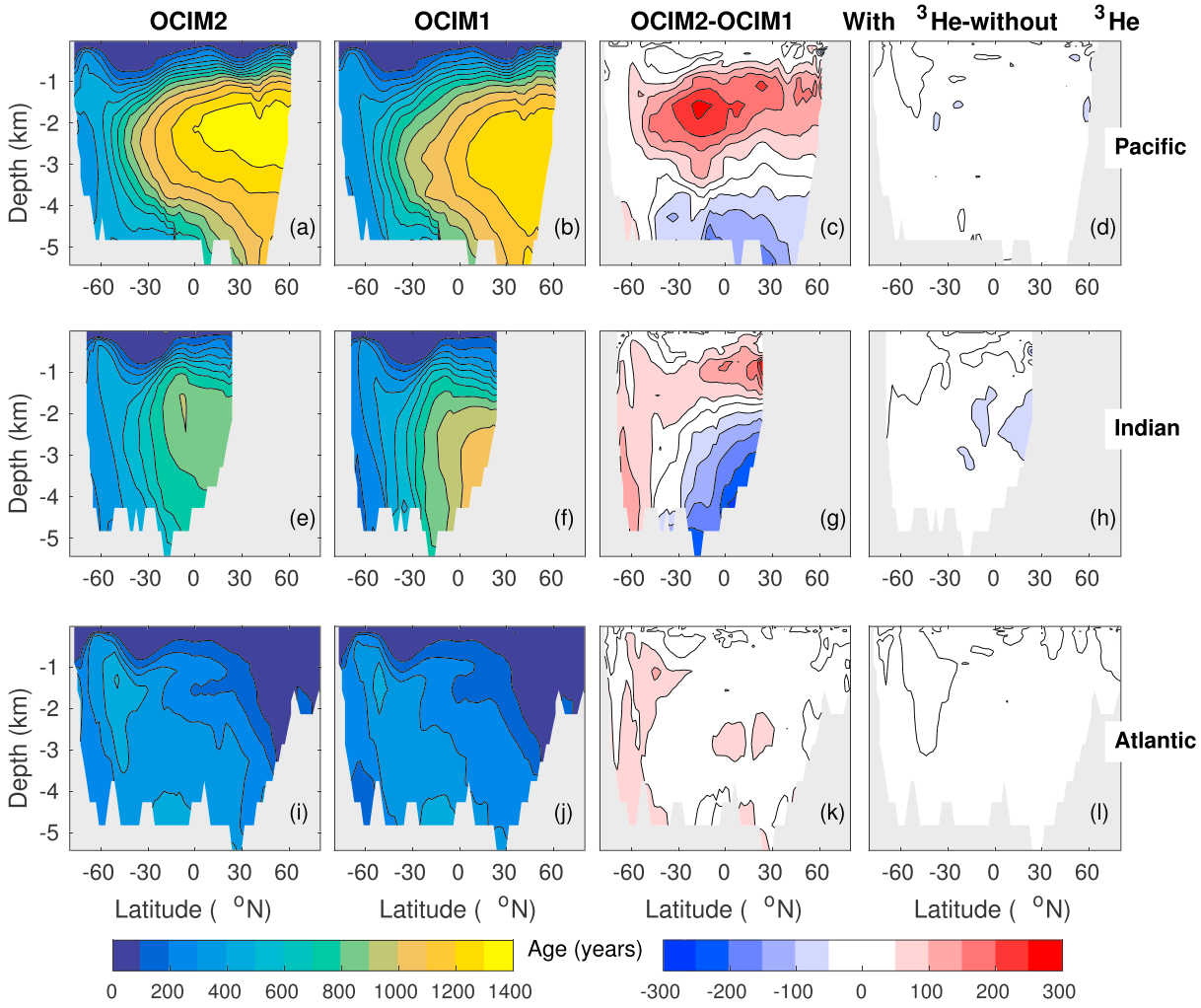

Figure 5. Zonally basin-averaged mean time since last ventilation (ideal mean age) in OCIM2 (a, e, and i) and OCIM1 (b, f, and j), for the Pacific (a–d), Indian (e–h), and Atlantic (i–l) Oceans. Also shown is the difference in mean age between OCIM2 and OCIM1 (c, g, and k), as well as the difference between two versions of OCIM2, one with and one without δ^3He constraints (d, h, and l). OCIM = ocean circulation inverse model.

The ideal mean age of a water parcel at a given location is defined as the mean time elapsed since the fluid elements of the parcel were last in contact with the surface mixed layer. The ideal mean age calculated using OCIM2 transport is 100–300 years in the deep North Atlantic and 300–500 years in the Southern Ocean, reaching a maximum of ~1,300–1,400 years in the poorly ventilated middepth North Pacific (Figures 5a, 5e, and 5i). Compared to OCIM1, which was constrained by GLODAP Δ^{14}C (Figures 5b, 5f, and 5j), OCIM2 transport allows for older waters in the middepth Pacific and Indian Ocean, and in the Southern Ocean. The largest differences occur in the middepth Pacific (1,000- to 3,000-m depth), where OCIM2 ideal mean ages are up to 200–300 years older than the corresponding OCIM1 ages (Figure 5c). The Southern Ocean waters of OCIM2 are about 50–100 years older than in OCIM1, in line with their lower Δ^{14}C values (see Figure 1). OCIM2 predicts significantly younger waters in the deep Pacific and Indian Oceans, with ideal mean ages 50–200 years younger than those predicted by OCIM1 (Figures 5c and 5g). Deep waters in the Atlantic Ocean are roughly the same age in OCIM2 and OCIM1 (Figure 5k). The patterns of the ideal mean age, and the age differences between OCIM2 and OCIM1, are robust to changes in the isopycnal and diapycnal diffusivities, with uncertainties (quantified by half the ensemble range) of 50–100 years or less, or about 30% of the differences shown in Figures 5c, 5g, and 5k.

To quantify the influence of δ^3He constraints on the assimilated ventilation ages, we compared the ideal mean age in the OCIM2 with and without δ^3He included in the assimilation. The results show essentially no difference between the versions of the model with and without the assimilation of δ^3He (Figures 5d,

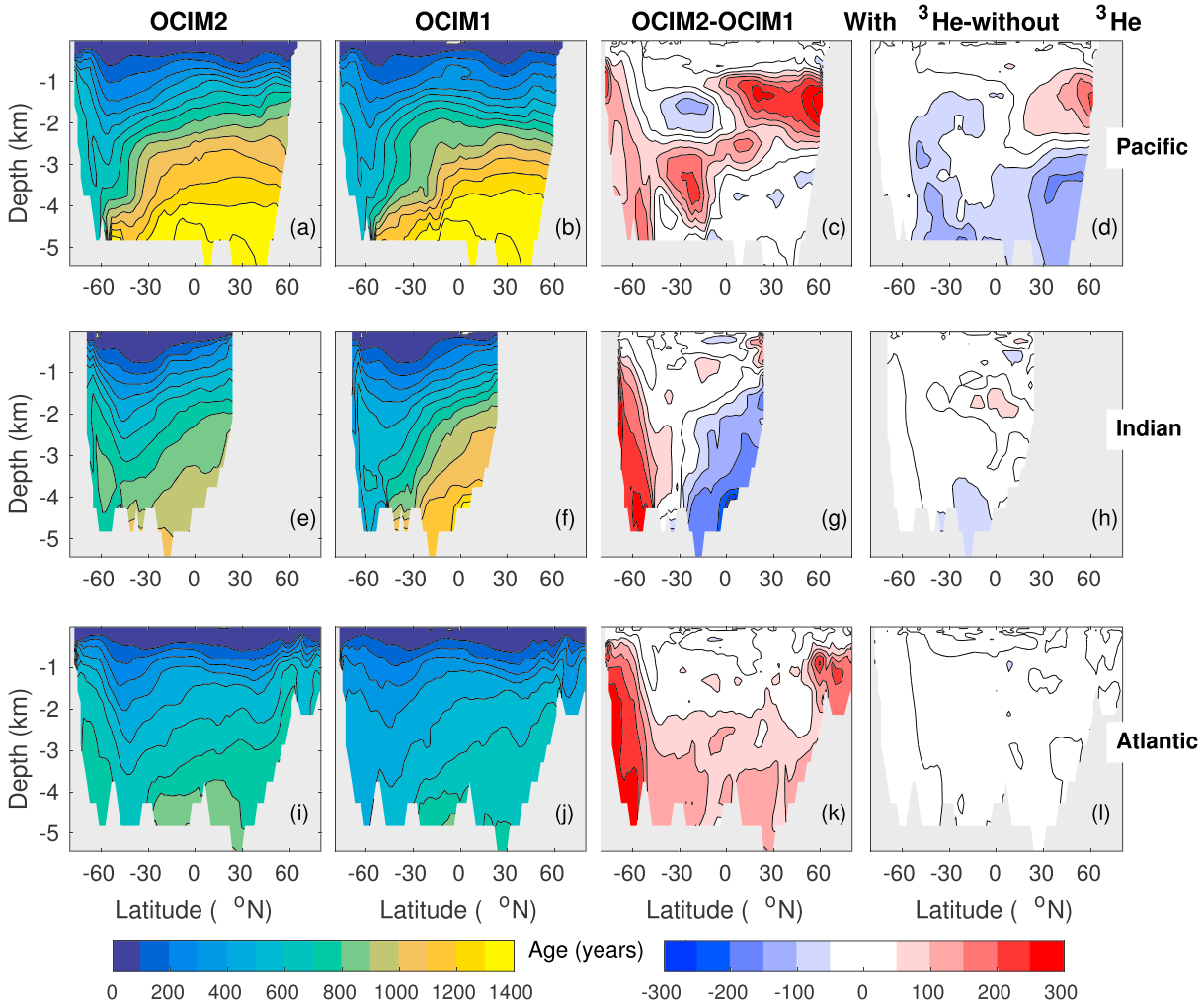

Figure 6. Zonally basin-averaged mean time since next ventilation (mean reexposure time) in OCIM2 (a, e, and i) and OCIM1 (b, f, and j), for the Pacific (a–d), Indian (e–h), and Atlantic (i–l) Oceans. Also shown is the difference in the mean reexposure time between OCIM2 and OCIM1 (c, g, and k), as well as between two versions of OCIM2, one with and one without δ^3He constraints (d, h, and l). OCIM = ocean circulation inverse model.

5h, and 5i). This indicates that δ^3He does not provide a strong constraint on ideal mean age beyond that already provided by the other assimilated tracers, primarily Δ^{14}C. The sensitivity of these age differences to variations in the isopycnal and diapycnal diffusivities is negligible.

Next, we consider the mean reexposure time, which is the mean time until the fluid elements of a given water parcel make next contact with the surface mixed layer. Like the ideal mean age, the mean reexposure time increases along the deep ocean conveyor circulation (Holzer & Primeau, 2008) from relatively short times in the deep North Atlantic to long times in the deep North Pacific, where the mean reexposure time reaches a maximum of >1,400 years (Figures 6a, 6e, and 6i). Unlike the ideal mean age, however, which has a maximum at middepths, the mean reexposure time is longest for bottom waters. Differences between the OCIM2 and OCIM1 reexposure times (Figures 6c, 6g, and 6k) show some similarities to the differences observed for the ideal mean age (Figures 5c, 5g, and 5k). Mean reexposure times are longer in OCIM2 than in OCIM1 in most regions, particularly in the Southern Ocean and middepth North Pacific, where the differences are >200 years in some locations. Mean reexposure times in OCIM2 are shorter than those in OCIM1 in the deep Indian Ocean, where the OCIM2 values are ~100–200 years less than OCIM1 (Figure 6g), and in the middepth South Pacific at ~1,000–2,000 m where the differences are ~50–100 years (Figure 6c). The mean reexposure times have uncertainties (associated with the uncertain subgrid diffusivities) of 50–150 years, and the differences between OCIM2 and OCIM1 have uncertainties of ~25–75 years, or roughly 30% of the differences illustrated in Figures 6c, 6g, and 6k.

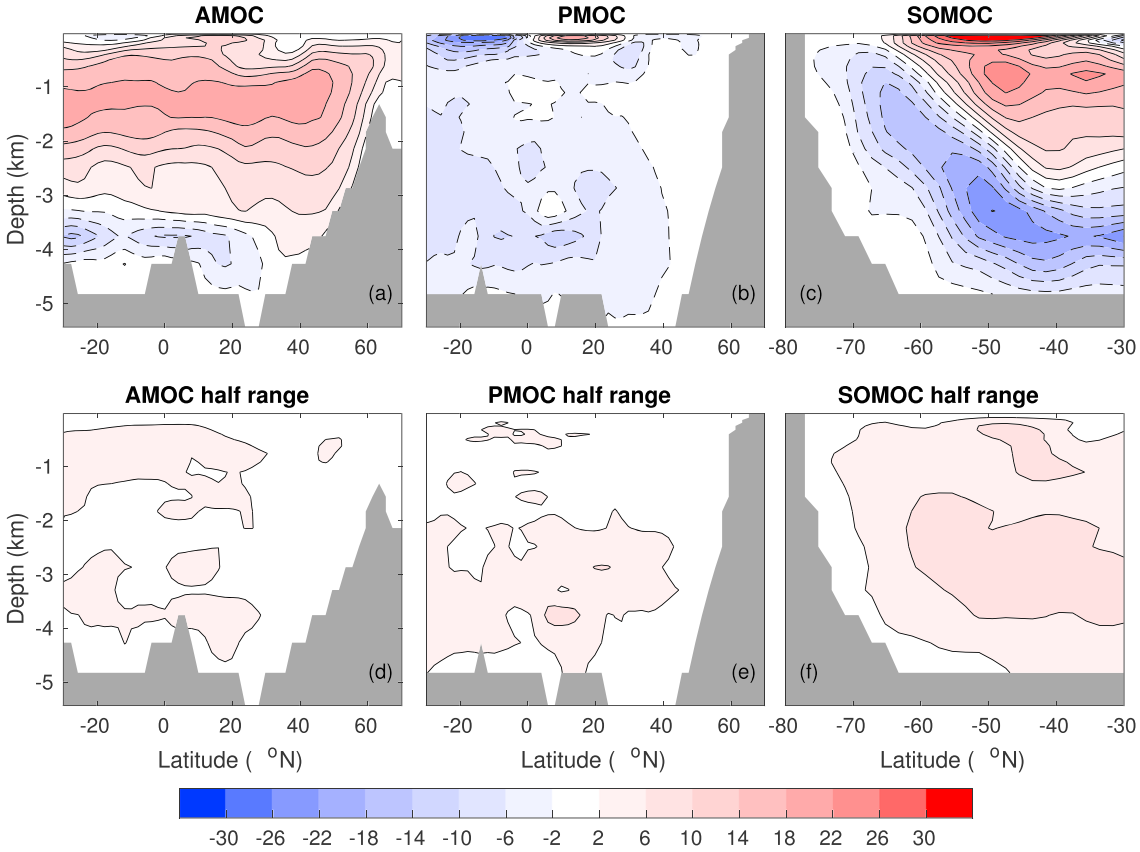

Figure 7. Meridional overturning streamfunction (positive = clockwise circulation, negative = counterclockwise circulation) for the Atlantic meridional overturning circulation (AMOC, panel a), Pacific meridional overturning circulation (PMOC, panel b), and Southern Ocean meridional overturning circulation (SOMOC, panel c) for OCIM2, averaged across the ensemble of diffusivity cases considered. Panels (d)–(f) show half the range of the meridional overturning circulation across the ensemble, illustrating the sensitivity of the optimized overturning to the choice of subgrid-scale diffusivity. The contour interval is 4 Sv in all figures, with the first contour at ±2 Sv (panels a–c) and 2 Sv (panels d–f).

Assimilating δ^3He in OCIM2 has a substantial effect on the inferred mean reexposure times, particularly in the Pacific Ocean. Including the δ^3He constraint reduces the mean time for deep Pacific waters to reach the surface by 50–150 years (Figure 6d). In the middepth North Pacific at ~1,000- to 2,000-m depth, assimilating δ^3He increases the mean time to next ventilation by 50–200 years (Figure 6d). These differences are very robust across the suite of sensitivity runs, with uncertainties of 25–50 years at most, or about 25% of the differences illustrated in Figures 6d, 6h, and 6l.

Overall, we find that assimilating δ^3He data affects the mean time to next ventilation, but not the mean time since last ventilation (compare Figures 5d, 5h, and 5l and Figures 6d, 6h, and 6l). Thus, δ^3He provides important information on interior-to-surface transport not captured by Δ^{14}C. This reflects the fact that δ^3He has an interior source and a surface sink, while the opposite applies to Δ^{14}C. Used in combination, Δ^{14}C and δ^3He provide strong constraints on deep ocean ventilation, with Δ^{14}C constraining both last- and next ventilation times, and δ^3He providing information on next ventilation times.

3.4. Large-Scale Circulation

The meridional overturning circulation of the Atlantic (AMOC), Pacific MOC (PMOC), and Southern Ocean (Figure 7) are in general agreement with other estimates from observations and inverse models (Table 2). The overturning strength of the AMOC is ~20 Sv in both the OCIM2 and OCIM1, in rough agreement with observations from satellite altimetry and underwater cables (Frajka-Williams, 2015), as well as hydrographic inverse models (Lumpkin & Speer, 2007; Table 2). (Here and elsewhere, the overturning stream function is referenced to 0 Sv at the seafloor.) The AMOC strength is essentially the same in OCIM2 and OCIM1 and has little sensitivity to either the subgrid-scale diffusivities (Figure 7d) or to the inclusion of δ^3He in the assimilation (Table 2). This indicates that the strength of the AMOC is well constrained by the hydrographic

Table 2
Representative Overturning Strengths and Volume Transports Predicted by OCIM2 and OCIM1, Compared to Some Previous Estimates

Location	OCIM2	OCIM1	Previous estimates	Reference
Atlantic MOC at 24–26°N	21 ± 2 (0.4 ± 1)	20 ± 1	17 ± 2	Frajka-Williams (2015)
			18 ± 3	Lumpkin and Speer (2007)
Southern Ocean MOC at 32°S	22 ± 7 (−0.8 ± 1.5)	16 ± 1	21 ± 7	Lumpkin and Speer (2007)
			22	Talley (2003)
Pacific Ocean MOC at 24°N	8 ± 5 (3 ± 5)	6 ± 1	5 ± 3	Lumpkin and Speer (2007)
Drake Passage transport	153 ± 6 (2 ± 4)	151 ± 3	173 ± 11	Donohue et al. (2016)
(66–70°W, 57–65°S)			153 ± 5	Mazloff et al. (2010)
			134 ± 20	Cunningham et al. (2003)
Indonesian Throughflow transport	−10 ± 1 (−0.2 ± 1)	−12 ± 1	−15 ± 4	Sprintall et al. (2009)
(124–132°E, 3°S), (108–110°E, 5°S)			−9 ± 1	Vranes et al. (2002)

Note. In the OCIM2 column, the numbers in parentheses represent the difference between the OCIM2 with and without δ^3He assimilation. Uncertainties are half the ensemble range. Units are in sverdrups (10^6 m^3/s). OCIM = ocean circulation inverse model.

data (including CFCs), as well as the constraints imposed by surface heat and freshwater fluxes and sea surface height, all of which are assimilated by both OCIM2 and OCIM1.

The lower limb of the global overturning circulation in the Southern Ocean has a maximum overturning of 22 ± 7 Sv at 32°S (Figure 7c and Table 2), in broad agreement with previous estimates derived from hydrographic data (Lumpkin & Speer, 2007; Talley, 2003). The uncertainty in the deep overturning stems from sensitivity to the subgrid diffusivities (Figure 7f): The global meridional overturning circulation (MOC) at 32°S has a minimum value of 17 Sv for the HIGH-ISO case and a maximum of 31 Sv for the HIGH-DIA + LOW-ISO case. The inclusion of the HIGH-DIA cases in the OCIM2 ensemble accounts for most of the discrepancy between the OCIM2 and OCIM1 estimates of Southern Ocean overturning, with OCIM1 estimating a weaker bottom cell (16 ± 1 Sv at 32°S; Table 2). The assimilation of δ^3He data has a variable effect on the Southern Ocean MOC, with some diffusivity cases showing weaker and some stronger overturning, but overall, the effect is negligible (Table 2).

The overturning circulation of the Pacific Ocean is much weaker than that in the Atlantic or Southern Oceans and consists of a relatively weak inflow of dense bottom waters from the Southern Ocean, which are converted to lighter waters by diapycnal mixing near the seafloor and geothermal heating (de Lavergne et al., 2017; Emile-Geay & Madec, 2009; Lumpkin & Speer, 2007). It is not our goal here to resolve or diagnose all of the mechanisms of buoyancy conversion in the deep Pacific waters. A caveat of our model is that geothermal heating is not included, and therefore, its effects on the buoyancy conversion of deep waters must be accounted for by adjustments to the momentum balance. Nonetheless, our suite of OCIM2 simulations captures a roughly 6- to 10-Sv overturning in the deep Pacific (Figure 7b). The deep Pacific overturning is 8 ± 5 Sv at 24°N and reduces to 2 ± 1 Sv at 48°N, in agreement with a previous hydrographic inverse model which found an overturning of 5 ± 3 and 2 ± 2 Sv at those latitudes (Lumpkin & Speer, 2007). (The large uncertainties in the deep Pacific overturning at 24°N stem mainly from the single HIGH-ISO model that was included in the ensemble: If we exclude that model, the overturning at 24°N is 6 ± 1 Sv.) As expected from the important role of diapycnal mixing in the conversion of dense bottom waters to lighter waters in the Pacific, the PMOC is highly sensitive to the value of the diapycnal diffusivity (Figure 7e). The half-range of the PMOC from our suite of sensitivity runs is ~2–4 Sv in the deep Pacific, or about 30–50% of the mean overturning. Similar sensitivity has been observed in dynamical models (Friedrich et al., 2011; Furue & Endoh, 2005). The assimilation of δ^3He observations has a substantial but uncertain effect on the deep PMOC, increasing it by 3 ± 5 Sv at 24°N relative to the OCIM2 models without δ^3He constraints (Table 2). Again, the large uncertainty is driven mainly by the HIGH-ISO simulation: If we exclude that model, the δ^3He constraints enhance the deep PMOC at 24°N by 1 ± 1 Sv.

Overall, we find that the MOC in the Pacific and Southern Oceans is quite sensitive to the values of subgrid-scale diffusivities (particularly $\kappa_\perp$), with sensitivities to the inclusion of δ^3He in the assimilation being of secondary importance. Most previous estimates put the deep ocean diapycnal diffusivity at $(1 - 4) \times 10^{-4}$ m^2/s (Ganachaud, 2003; Lumpkin & Speer, 2007; Macdonald et al., 2009; Talley, 2003), although turbulent diapycnal diffusivities as large as 10^{-3} m^2/s near the ocean bottom have been inferred from models of tidal mixing and internal wave breaking (Nikurashin & Ferrari, 2013). On the other hand, diapycnal diffusivities inferred from acoustic doppler current profilers show $\kappa_\perp \leq 10^{-5}$ m^2/s over much of the ocean interior, approaching and rarely exceeding 10^{-4} m^2/s near rough topography, with very large spatial heterogeneity (Kunze et al., 2006). In agreement with these smaller diffusivities, a recent inverse model of the abyssal circulation in the northeast Pacific found $\kappa_\perp < 10^{-5}$ m^2/s over most of the domain (Hautala, 2018). Our sensitivity analyses are rather crude approximations of the minimum and maximum potential values of $\kappa_\perp$ at large scales in the interior ocean and thus only provide a rough bound on the potential range of the MOC in different basins. Accurate estimates of the MOC from inverse models such as the OCIM will require a detailed model of the geographical distribution of $\kappa_\perp$, and to a lesser extent of $\kappa_\parallel$, which we leave to future work.

Other large-scale transports through important choke points between basins are relatively insensitive to the values of subgrid-scale diffusivities, or to the δ^3He assimilation. The transport through Drake Passage in OCIM2 is relatively well constrained at 153 ± 6 Sv, which is in line with the OCIM1 estimate of 151 ± 3 Sv. Both values are higher than the canonical Drake Passage transport of 134 ± 20 Sv estimated by Cunningham et al. (2003), but nearly identical to that found by the Southern Ocean State Estimate for the years 2005–2006 (Mazloff et al., 2010), and lower than a recent estimate based on current-meter observations for the period 2007–2011 (Donohue et al., 2016; Table 2). Assimilating δ^3He data into OCIM2 increases the Drake Passage transport by only 2 ± 4 Sv. Like the AMOC, the strength of the Drake Passage transport appears to be well constrained by the hydrographic data (including CFCs), sea surface height, and surface fluxes of heat and freshwater, and shows little sensitivity to the assimilation of δ^3He data. For the Indonesian Throughflow (ITF), OCIM2 predicts a weaker ITF (10 ± 1 Sv) than OCIM1 (12 ± 1 Sv), which falls at the lower end of previous observation-based estimates that range from ~9–15 Sv (Sprintall et al., 2009; Vranes et al., 2002).

In terms of the horizontal velocity field of the deep ocean (Figure 8 shows the stream function of its non-divergent and dominant component), the major circulation features at 2,500-m depth are the Antarctic Circumpolar Current, separating cyclonic flow to the south of ~45°S and anticyclonic flow to the north, and the deep western boundary current of the Atlantic (Figure 8a). In addition, OCIM2 features strong circulations in the deep Eastern Tropical Pacific that are enhanced in the models constrained by δ^3He (Figures 8a and 8b). The broad anticyclonic flow between 15°S and 30°S is consistent with previous inverse models of the deep circulation in the southeast Pacific (Faure & Speer, 2012; Hautala & Riser, 1993) and with the observed propagation of δ^3He plumes at 15°S (westward) and 28°S (eastward). It is also consistent with the circulation patterns predicted by dynamical models of hydrothermal forcing, which for the Southern Hemisphere predict an anticyclonic gyre at the depth of ^{3}He injection (Faure & Speer, 2012; Stommel, 1982). Westward velocities in the core of the δ^3He plume at ~15°S are 0.7 ± 0.2 cm/s in the OCIM2, with the uncertainty stemming from the sensitivity to the value of subgrid-scale diffusivity. These velocities are a bit higher than previous hydrographic inverse models that estimated westward velocities of 0.2–0.5 cm/s in this region (Faure & Speer, 2012; Hautala & Riser, 1993).

Assimilating δ^3He into OCIM2 produces more pronounced circulations in the equatorial deep Pacific (Figures 8a and 8b), with counterclockwise flow centered on the equator and clockwise flow centered on ~5°N and ~5°S. These streamlines suggest jet-like zonal currents in the deep equatorial Pacific, with eastward flow south of the equator and westward flow to the north (Figure 8a). However, it is important to note that the tropical currents featured in OCIM2 (Figure 8a) carry significant uncertainty: The sensitivity of the streamflow to variations in the diffusivity is ~50% of the mean (Figure 8c). Furthermore, the coarse resolution of OCIM2 is unlikely to capture all of the important features of deep equatorial currents.

In general, the regional-scale aspects of the deep and abyssal currents determined by OCIM2 are sensitive to the values of the subgrid-scale diffusivities. For example, in the northeast Pacific at 165–169°W, we find westward flow north of 41°N and eastward flow south of 41°N in the models that use a small background value of $\kappa_\perp = 10^{-5}$ m^2/s in the interior ocean, in agreement with the circulation pattern inferred by Hautala (2018) who also inferred $\kappa_\perp < 10^{-5}$ m^2/s in this region. In the HIGH-DIA models, on the other hand, we

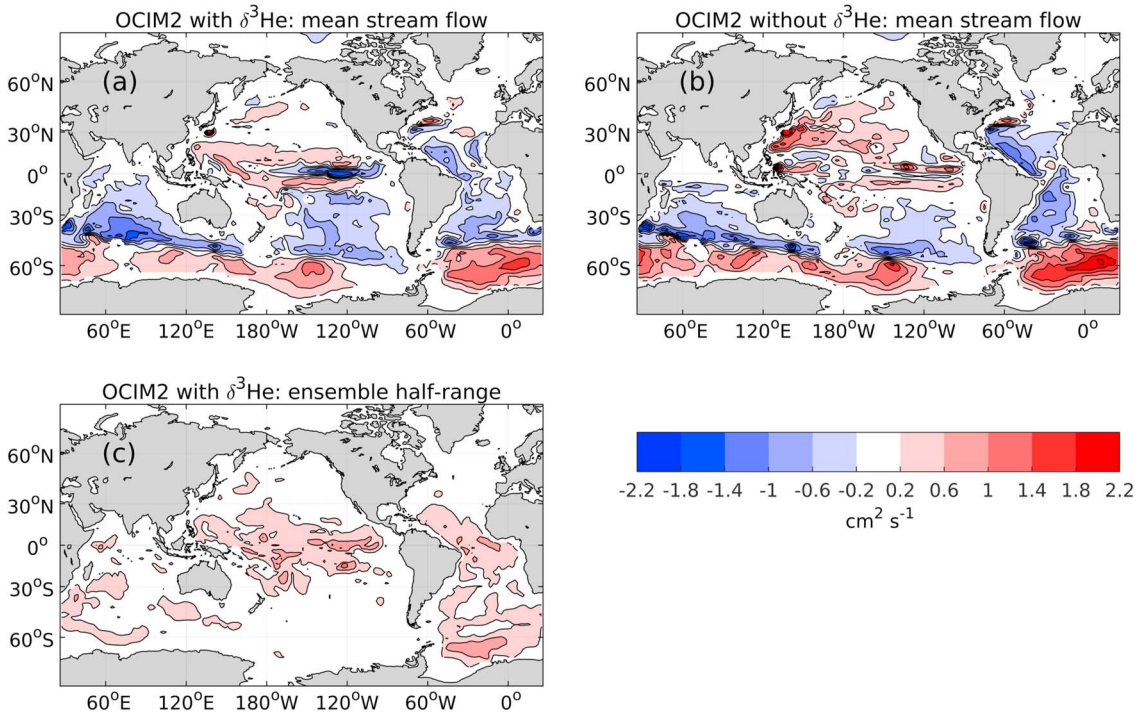

Figure 8. The stream function (positive = clockwise circulation, negative = counterclockwise circulation) of the nondivergent component of the horizontal velocity at 2,500-m depth in OCIM2, averaged across the ensemble (panel a). (b) The same as (a) but for the version of OCIM2 without δ^3He constraints. (c) The half-range of the stream function across the ensemble, illustrating the sensitivity of the stream function to the choice of subgrid-scale diffusivity. The contour interval is 0.4 cm^2/s, straddling zero symmetrically. OCIM = ocean circulation inverse model.

find that the lateral abyssal circulation in the northeast Pacific is reversed, with eastward flow north of 41°N and westward flow south of 41°N. The lesson here is that while the mean ventilation times and pathways of the deep ocean are robust and well constrained by the tracer data, the details of the interior velocity field, especially in quiescent regions, are highly sensitive to the model diffusivities. Therefore, accurately resolving the detailed interior circulation pathways will require knowledge of both diapycnal and isopycnal diffusivities and their geographic variation. This is left to future work.

3.5. Mantle ^{3}He Sources

A further contribution of this work is a new estimate of mantle-^{3}He sources that is consistent with the distribution of δ^3He in the ocean (Figure 9a). The mantle-^{3}He sources in the model are located along known ridge spreading centers as specified in the OCMIP2 protocol (Dutay et al., 2004). The depth of mantle-^{3}He injection also follows the OCMIP2 protocols, which is roughly 300 m above the ridge axis to approximate the buoyant rising of hydrothermal vent waters. However, unlike the OCMIP2 protocol, we do not specify a globally integrated mantle-^{3}He source nor do we tie the mantle-^{3}He source to the ridge spreading rate. Instead, the local mantle-^{3}He injection rate of every source grid box is determined as part of the solution to our inverse model, to provide an optimal fit to the observed δ^3He distribution. Our inversion finds that the lowest local rates of mantle-^{3}He injection occur in the North Atlantic and South Indian Oceans (Figure 9a). However, the source estimates for the North Atlantic must be interpreted with caution because our inversion did not use the δ^3He observations in that region to avoid contamination by tritiugenic ^{3}He. The largest local hydrothermal ^{3}He sources occur in the southeast Pacific and northeast Pacific along the EPR and in the Pacific sector of the Southern Ocean (Figure 9a).

The globally integrated source of mantle ^{3}He ranges from 585 to 672 mol/year across our suite of sensitivity experiments. All of the models infer mantle-^{3}He sources significantly lower than the 1,000-mol/year OCMIP2 source and much closer to a more recent estimate of 527 ± 102 mol/year based on objective mapping of excess ^{3}He in the ocean (Bianchi et al., 2010; Figure 9c). Our estimates are also lower than a recent estimate of 760–850 mol/year, which was based on optimizing regionally integrated ^{3}He sources to match δ^3He concentrations using the OCIM1 circulations (Holzer et al., 2017). Holzer et al. (2017) additionally

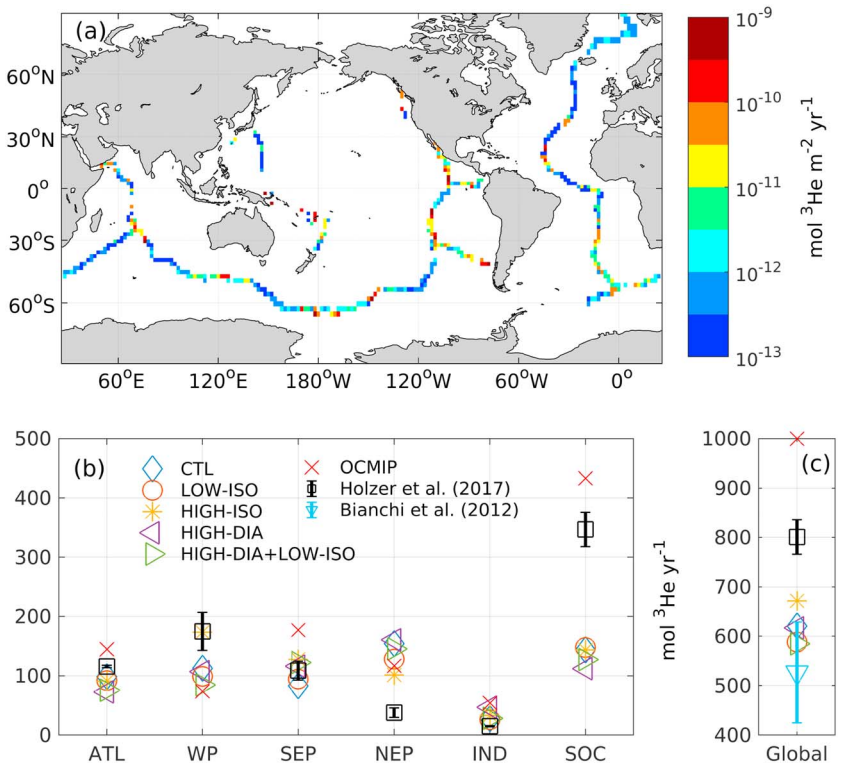

Figure 9. Ensemble-averaged global distribution of mantle-^{3}He sources along ocean spreading ridges in OCIM2 (a), and regionally integrated (b) and globally integrated (c) mantle-^{3}He sources for the different ensemble members, compared to source estimates from three previous studies. The regions are as follows: ATL = Atlantic; WP = Western Pacific; SEP = Southeastern Pacific; NEP = Northeastern Pacific; IND = Indian; SOC = Southern Ocean; OCIM = ocean circulation inverse model.

improved the fit to observed δ^3He by optimizing the vertical injection profile of hydrothermal fluid, which moved the mean injection depth up by roughly a grid layer. Using the prescribed OCMIP injection depth as done here, Holzer et al. (2017) estimated a source of 720–780 mol/year for the OCIM1 circulations. Here we jointly optimized the circulation and the grid-scale mantle-^{3}He sources, which allows a closer match to δ^3He observations and perhaps a more accurate mantle-^{3}He source estimation, at the expense of spatial smoothness in the injection rates.

Examining regionally integrated mantle-^{3}He sources (Figure 9b), it is clear that the major difference between this and previous studies lies in the Southern Ocean, where OCIM2 estimates a source of 112–148 mol/year, compared to 433 mol/year for OCMIP2 and 350 ± 30 mol/year as estimated by Holzer et al. (2017). Our model also finds weaker sources in the Atlantic Ocean and southeast Pacific (73–99 and 83–128 mol/year, respectively) compared to the OCIMP2 source (145 and 177 mol/year, respectively). One region where our model consistently predicts stronger sources than OCMIP2 is the western Pacific (85–174 mol/year in our model compared to 74 mol/year in OCMIP2). These higher sources are located southeast of Fiji near (20°S, 175°W) and southeast of Papua New Guinea (Figure 9a). The former site is near the Lau Basin, and the latter lies in the Woodlark Basin, both of which are known to contain active hydrothermal vent systems (e.g., Fouquet et al., 1990; Lisitsyn et al., 1991). Previous modeling studies have also shown that the Lau Basin must have larger mantle-^{3}He sources than specified by OCMIP2 in order to match the observed δ^3He distribution in the southwest Pacific (Schlitzer, 2016). For the northeast Pacific ridge system, most ensemble members (except for HIGH-ISO) predict higher mantle-^{3}He sources than OCMIP2. The northeast Pacific mantle-^{3}He sources are also much higher than those inferred using the OCIM1 circulation (Holzer et al., 2017), which can be traced back to biases in the OCIM1 ventilation of North Pacific deep waters (Holzer et al., 2017).

The precise value of the inferred mantle-^{3}He source, as well as its regional distribution, depends on the value of the subgrid-scale diffusivity employed in the model. The smallest sources are found in the LOW-ISO models and the largest source in the HIGH-ISO model (Figure 9c). This reflects the fact that a larger isopy-

cnal diffusivity will ventilate the densities around the mean injection depth at a higher rate where they outcrop in the Southern Ocean, requiring higher sources to match the observed δ^3He. The sensitivity of the mantle-^{3}He source to the diffusivity is modulated by the optimized air-sea gas exchange piston velocity, which governs how much isotopically light atmospheric helium enters the ocean. The global mean of the piston velocity parameter γ is 0.251 cm·hr^{-1}·m^2·s^{-2} with very little variation across the ensemble, in agreement with value estimated by Wanninkhof et al. (2013). But in the Southern Ocean (south of 40°S), where much of the ocean's deep waters are ventilated, γ ranges from 0.167 in the HIGH-ISO model to 0.240 in the LOW-ISO model. Assuming that the true value of γ is closer to the higher values, this most likely indicates that the large globally uniform isopycnal diffusivities of the HIGH-ISO model (2,000 m^2/s) are not realistic and the true values are smaller on average. The LOW-ISO models overall support a slightly lower global mantle-^{3}He source, with a slightly higher percentage emanating from Southern Ocean vents.

One important motivation for improving estimates of mantle-^{3}He sources and the transport of ^{3}He away from vent locations is to better estimate hydrothermal sources of trace metals and their transport to the surface ocean. Recent ship transects have found large plumes of dissolved trace metals such as iron (Fe) and zinc (Zn) emanating from active hydrothermal vents (e.g., Fitzsimmons et al., 2014; Resing et al., 2015; Roshan et al., 2016). These trace metals are important micronutrients that sustain phytoplankton in the surface ocean. It has been hypothesized on the basis of model simulations that Fe from hydrothermal vents may support up to 30% of net primary productivity in the Southern Ocean (Resing et al., 2015). Recent inverse modeling has shown that currently available observations of dissolved iron are consistent with a range of hydrothermal iron source strengths that support anywhere from near zero to ~20% of the global export production (Pasquier & Holzer, 2017). Our estimates suggest that the mantle-^{3}He sources of the Southern Ocean may be weaker than previously thought. This could translate to lower supply rates of hydrothermal trace metals to the Southern Ocean surface, where these metals have the greatest potential for impacting biological productivity, given the low supply from atmospheric dust deposition (Tagliabue et al., 2010). However, the full impact of hydrothermal vents on surface productivity is also determined by the metal:^{3}He ratio, which varies substantially from one vent location to another (e.g., Saito et al., 2013).

4. Remaining Uncertainties

Several sources of uncertainty remain in the inverse solution. The largest source of uncertainty in the inferred circulation field is the values of the subgrid-scale diffusivities, which are known to have very large geographic variations (Kunze et al., 2006) that are not captured by the OCIM. Over the range of diffusivities explored here, the meridional overturning circulation varies by roughly 50% in the deep Pacific and by ~30% in the Southern Ocean. We also find that regional-scale flows in the deep ocean are sensitive to the magnitude of the diffusivity.

Inferred mantle-^{3}He sources are also sensitive to the diffusivity values, as well as the Southern Ocean air-sea piston velocity. It is important to keep in mind that the OCIM does not simulate seasonal variability in circulation or air-sea gas exchange, which could be particularly important in the Southern Ocean where sea ice extent and deep water formation is highly seasonal. It is difficult to predict how a more realistic distribution of diffusivities, combined with resolution of seasonal variations in air-sea gas exchange, would affect our inferred mantle-^{3}He sources, but the Southern Ocean mantle-^{3}He sources are likely the most sensitive to these variables. Higher ventilation rates associated with higher upper-ocean eddy diffusivity and summertime ice-free gas exchange, combined with lower deep ocean diffusivities, may be consistent with realistic gas exchange and higher mantle helium sources. Future versions of the OCIM should include realistic spatially varying diapycnal and isopycnal diffusivities and resolve seasonality of circulation and gas exchange, in order to better constrain both the deep ocean circulation and the mantle-^{3}He sources.

Other potential sources of uncertainty include the neglect of minor sources of radiocarbon and helium isotopes that can affect the Δ^{14}C and δ^3He distributions. For radiocarbon, these sources include remineralization of organic matter produced in the surface ocean or transported from rivers and release of DIC from hydrothermal vents. Although these sources are small compared to the surface gas exchange, they may be important regionally and affect Δ^{14}C by up to 10% (Fiadeiro, 1982), which is larger than the model-data misfit (Figure 2). If some of the bomb-produced ^{14}C has penetrated into regions where there are no CFCs by the remineralization of sinking organic particles, then the natural (prebomb) Δ^{14}C in intermediate-depth and

Southern Ocean waters should be even lower (older) than it is for OCIM2, which would require an even larger correction to the original GLODAP prebomb $\Delta^{14}C$ product (Figures 1 and 2).

For helium isotopes, we neglected for simplicity a source of ^3He from the decay of naturally occurring tritium (Bayer & Schlosser, 1991) and a source of ^4He from crustal sediments (Well et al., 2001). The ^3He source from natural tritium would tend to produce higher δ^3He values and is likely most important in recently ventilated waters, while the crustal ^4He source would tend to produce lower δ^3He values and is likely most important in older waters such as the North Pacific (Well et al., 2001). The effect of neglecting these sources on the inferred mantle-^3He injection rates is likely smaller than the uncertainties due to the subgrid-scale diffusivities reported here.

Lastly, the coarse vertical resolution of the OCIM is another source of unquantified uncertainty. The 24 levels currently used may be insufficient to resolve some features of the deep circulation and may alias the vertical distribution of mantle helium sources. Future work should focus on improving the resolution of the model particularly near topographic features.

5. Conclusions

We presented a new version of the OCIM (DeVries, 2014), referred to here as OCIM2, that provides improved estimates of deep ocean ventilation and circulation by assimilating helium isotope and radiocarbon observations. Our key findings are the following:

1. OCIM2 provides a better fit to the raw deep ocean radiocarbon data (screened for possible bomb contamination), improving on previous versions that used GLODAP-mapped radiocarbon. The GLODAP prebomb radiocarbon product was demonstrated to contain systematic errors; the OCIM2-inferred natural radiocarbon field provides an alternative that is free of these errors.
2. OCIM2 predicts waters that are more slowly ventilated in the Southern Ocean and middepth Pacific and more rapidly ventilated in the deep Pacific and Indian Oceans. Compared to the previous model version, changes in mean ventilation times are as large as several hundred years. Assimilating δ^3He influences the mean time to next ventilation, with reductions in the deep Pacific Ocean of 50–150 years.
3. Assimilating δ^3He reorganizes the deep circulation to capture δ^3He plumes with realistic structure. Specifically, the large plume emanating from the EPR at ~15°S shows dominant westward propagation, a feature that has eluded previous modeling studies. The effect of the δ^3He constraints on the deep overturning circulation is only a small, uncertain strengthening by a few sverdrups.
4. OCIM2 infers an optimized globally integrated mantle helium source of 585–672 mol/year. This lies in the middle of previous data-based estimates, which span a range of ~450–850 mol/year (Bianchi et al., 2010; Holzer et al., 2017; Schlitzer, 2016). The largest regional difference occurs in the Southern Ocean where the OCIM2 mantle-^3He source is up to threefold lower than previous estimates.

Circulation inverse models such as OCIM2 provide accurate large-scale tracer transport. The assimilated steady and transient tracer constraints ensure that simulated tracers (including those not assimilated) have realistic large-scale distributions and that ventilation time scales are accurately captured. This feature makes the OCIM invaluable for biogeochemical studies for which it has been widely used (e.g., DeVries & Weber, 2017; Roshan & DeVries, 2017; Weber et al., 2018). However, because of its inverse nature, a large range of subgrid-scale diffusivities can be accommodated with very similar fidelity to the assimilated tracer and dynamical fields. This is accomplished through optimal adjustments in the velocity field that compensate for deficiencies or unrealistic features in the diffusivity field. The resulting advective-diffusive transport produces realistic large-scale tracer fields and transport time scales, but the uncertainties in the diffusivities translate to uncertainties in the velocity field. As a result, regional advective circulation features, particularly where the ocean is relatively quiescent, have significant order-50% uncertainty (e.g., the horizontal structure of the tropical deep Pacific circulation, Figure 8).

Given the nature of the OCIM's remaining uncertainties, we think that future work should focus on including realistic, spatially varying diffusivities and on enhancing model resolution, particularly in the vertical. Further improvements in both the formulation of the inverse model and in the spatial data coverage should allow more accurate ocean state estimates that fully exploit the information contained in deep ocean radiocarbon and helium isotope measurements.

Acknowledgments
T. D. acknowledges support from NSF grant OCE-1658392. The authors thank Bill Jenkins for providing the δ^3He data from the GEOTRACES GP16 transect and all the scientists whose data appear in the GLODAPv2 compilation. The data used are listed in the references.

References

Arakawa, A., & Lamb, V. R. (1977). Computational design of the basic dynamical processes of the UCLA general circulation model. *Methods in computational physics*, *17*, 173–265.

Bardin, A., Primeau, F., & Lindsay, K. (2014). An offline implicit solver for simulating prebomb radiocarbon. *Ocean Modelling*, *73*, 45–58.

Bayer, R., & Schlosser, P. (1991). Tritium profiles in the Weddell Sea. *Marine chemistry*, *35*(1-4), 123–136.

Bianchi, D., Sarmiento, J. L., Gnanadesikan, A., Key, R. M., Schlosser, P., & Newton, R. (2010). Low helium flux from the mantle inferred from simulations of oceanic helium isotope data. *Earth and Planetary Science Letters*, *297*(3), 379–386.

Broecker, W. S., Gerard, R., Ewing, M., & Heezen, B. C. (1960). Natural radiocarbon in the Atlantic Ocean. *Journal of Geophysical Research*, *65*(9), 2903–2931.

Bullister, J. L. (2015). *Atmospheric histories (1765–2015) for CFC-11, CFC-12, CFC-113, CCL4, SF6 and N_2O, Carbon Dioxide Information Analysis Center, Oak Ridge National Laboratory US Department of Energy*. Tennessee: Oak Ridge.

Craig, H. (1969). Abyssal carbon and radiocarbon in the Pacific. *Journal of Geophysical Research*, *74*(23), 5491–5506.

Cunningham, S., Alderson, S., King, B., & Brandon, M. (2003). Transport and variability of the Antarctic circumpolar current in Drake Passage. *Journal of Geophysical Research*, *108*, 8084. https://doi.org/10.1029/2001JC001147

de Lavergne, C., Madec, G., Roquet, F., Holmes, R. M., & McDougall, T. J. (2017). Abyssal ocean overturning shaped by seafloor distribution. *Nature*, *551*, 181–188. https://doi.org/10.1038/nature24472

DeVries, T. (2014). The oceanic anthropogenic CO_2 sink: Storage, air-sea fluxes, and transports over the industrial era. *Global Biogeochemical Cycles*, *28*, 631–647.

DeVries, T., & Primeau, F. (2010). An improved method for estimating water-mass ventilation age from radiocarbon data. *Earth and Planetary Science Letters*, *295*(3-4), 367–378.

DeVries, T., & Primeau, F. (2011). Dynamically and observationally constrained estimates of water-mass distributions and ages in the global ocean. *Journal of Physical Oceanography*, *41*(12), 2381–2401.

DeVries, T., & Weber, T. (2017). The export and fate of organic matter in the ocean: New constraints from combining satellite and oceanographic tracer observations. *Global Biogeochemical Cycles*, *31*, 535–555.

Donohue, K., Tracey, K., Watts, D., Chidichimo, M., & Chereskin, T. (2016). Mean Antarctic Circumpolar Current transport measured in Drake Passage. *Geophysical Research Letters*, *43*, 11,760–11,767. https://doi.org/10.1002/2016GL070319

Downes, S. M., Key, R. M., Orsi, A. H., Speer, K. G., & Swift, J. H. (2012). Tracing southwest Pacific bottom water using potential vorticity and helium-3. *Journal of Physical Oceanography*, *42*(12), 2153–2168.

Dutay, J.-C., Emile-Geay, J., Iudicone, D., Jean-Baptiste, P., Madec, G., & Carouge, C. (2010). Helium isotopic constraints on simulated ocean circulations: Implications for abyssal theories. *Environmental fluid mechanics*, *10*(1), 257–273.

Dutay, J.-C., Jean-Baptiste, P., Campin, J.-M., Ishida, A., Maier-Reimer, E., Matear, R. J., et al. (2004). Evaluation of OCMIP-2 ocean models' deep circulation with mantle helium-3. *Journal of Marine Systems*, *48*(1), 15–36.

Emile-Geay, J., & Madec, G. (2009). Geothermal heating, diapycnal mixing and the abyssal circulation. *Ocean Science*, *5*(2), 203–217.

Faure, V., & Speer, K. (2012). Deep circulation in the eastern South Pacific Ocean. *Journal of Marine Research*, *70*(5), 748–778.

Fiadeiro, M. E. (1982). Three-dimensional modeling of tracers in the deep Pacific Ocean 11. Radiocarbon and the circulation. *Journal of Marine Research*, *40*, 537–550.

Fitzsimmons, J. N., Boyle, E. A., & Jenkins, W. J. (2014). Distal transport of dissolved hydrothermal iron in the deep South Pacific Ocean. *Proceedings of the National Academy of Sciences*, *111*(47), 16,654–16,661.

Fouquet, Y., Charlou, J.-L., Donval, J., Foucher, J. P., Harmegnies, F., Pelle, H., et al. (1990). Hydrothermal activity in the Lau Basin: First results from the NAUTILAU Cruise. *Eos, Transactions American Geophysical Union*, *71*, 678–678.

Frajka-Williams, E. (2015). Estimating the Atlantic overturning at 26°N using satellite altimetry and cable measurements. *Geophysical Research Letters*, *42*, 3458–3464.

Friedrich, T., Timmermann, A., Decloedt, T., Luther, D., & Mouchet, A. (2011). The effect of topography-enhanced diapycnal mixing on ocean and atmospheric circulation and marine biogeochemistry. *Ocean Modelling*, *39*(3-4), 262–274.

Furue, R., & Endoh, M. (2005). Effects of the pacific diapycnal mixing and wind stress on the global and Pacific meridional overturning circulation. *Journal of Physical Oceanography*, *35*(10), 1876–1890.

Ganachaud, A. (2003). Large-scale mass transports, water mass formation, and diffusivities estimated from World Ocean Circulation Experiment (WOCE) hydrographic data. *Journal of Geophysical Research*, *108*(C7), 3213. https://doi.org/10.1029/2002JC001565

Garabato, A. C. N., Stevens, D. P., Watson, A. J., & Roether, W. (2007). Short-circuiting of the overturning circulation in the Antarctic Circumpolar Current. *Nature*, *447*(7141), 194.

Gebbie, G., & Huybers, P. (2012). The mean age of ocean waters inferred from radiocarbon observations: Sensitivity to surface sources and accounting for mixing histories. *Journal of Physical Oceanography*, *42*(2), 291–305.

Gnanadesikan, A., Dunne, J. P., Key, R. M., Matsumoto, K., Sarmiento, J. L., Slater, R. D., & Swathi, P. (2004). Oceanic ventilation and biogeochemical cycling: Understanding the physical mechanisms that produce realistic distributions of tracers and productivity. *Global Biogeochemical Cycles*, *18*, GB4010. https://doi.org/10.1029/2003GB002097

Gnanadesikan, A., Pradal, M.-A., & Abernathey, R. (2015). Exploring the isopycnal mixing and helium–heat paradoxes in a suite of Earth system models. *Ocean Science*, *11*(4), 591–605.

Godwin, H. (1962). Half-life of radiocarbon. *Nature*, *195*(4845), 984–984.

Graven, H., Gruber, N., Key, R., Khatiwala, S., & Giraud, X. (2012). Changing controls on oceanic radiocarbon: New insights on shallow-to-deep ocean exchange and anthropogenic CO_2 uptake. *Journal of Geophysical Research*, *117*, C10005. https://doi.org/10.1029/2012JC008074

Griffies, S. M., Gnanadesikan, A., Pacanowski, R. C., Larichev, V. D., Dukowicz, J. K., & Smith, R. D. (1998). Isoneutral diffusion in a *z*-coordinate ocean model. *Journal of Physical Oceanography*, *28*(5), 805–830.

Guilderson, T., Schrag, D., Fallon, S., Dunbar, R., Kilbourne, K., & Prouty, N. G. (2005). Surface Water Radiocarbon (Delta14C) Reconstructed from Reef-Building Zooxanthellate Corals from 1751-2004.

Hautala, S. L. (2018). The abyssal and deep circulation of the northeast Pacific basin. *Progress in Oceanography*, *160*, 68–82.

Hautala, S. L., & Riser, S. C. (1989). A simple model of abyssal circulation, including effects of wind, buoyancy and topography. *Journal of Physical Oceanography*, *19*(5), 596–611.

Hautala, S. L., & Riser, S. C. (1993). A nonconservative β-spiral determination of the deep circulation in the Eastern South Pacific. *Journal of Physical Oceanography*, *23*(9), 1975–2000.

Holzer, M., DeVries, T., Bianchi, D., Newton, R., Schlosser, P., & Winckler, G. (2017). Objective estimates of mantle 3-He in the ocean and implications for constraining the deep ocean circulation. *Earth and Planetary Science Letters*, *458*, 305–314.

Holzer, M., & Primeau, F. W. (2008). The path-density distribution of oceanic surface-to-surface transport. *Journal of Geophysical Research*, *113*, C01018. https://doi.org/10.1029/2006JC003976

Holzer, M., Primeau, F. W., Smethie, W. M., & Khatiwala, S. (2010). Where and how long ago was water in the western North Atlantic ventilated?, Maximum-entropy inversions of bottle data from WOCE line A20. *Journal of Geophysical Research*, *115*, C07005. https://doi.org/10.1029/2009JC005750

Holzer, M., Smethie, W., & Ting, Y.-H. (2018). Ventilation of the subtropical North Atlantic: Locations and times of last ventilation estimated using tracer constraints from GEOTRACES section GA03. *Journal of Geophysical Research: Oceans*, *123*, 2332–2352. https://doi.org/10.1002/2017JC013698

Jenkins, W. J., Lott, D. E., German, C. R., Cahill, K. L., Goudreau, J., & Longworth, B. (2017). The deep distributions of helium isotopes, radiocarbon, and noble gases along the U.S. GEOTRACES East Pacific Zonal Transect (GP16). *Marine Chemistry*, *201*, 167–182. https://doi.org/10.1016/j.marchem.2017.03.009

Jenkins, W., Lott, D., Longworth, B., Curtice, J., & Cahill, K. (2015). The distributions of helium isotopes and tritium along the US GEOTRACES North Atlantic sections (GEOTRACES GAO3). *Deep Sea Research Part II: Topical Studies in Oceanography*, *116*, 21–28.

Kalnay, E., Kanamitsu, M., Kistler, R., Collins, W., Deaven, D., Gandin, L., et al. (1996). The NCEP/NCAR 40-year reanalysis project. *Bulletin of the American Meteorological Society*, *77*(3), 437–472.

Kawabe, M., & Fujio, S. (2010). Pacific Ocean circulation based on observation. *Journal of Oceanography*, *66*(3), 389–403. https://doi.org/10.1007/s10872-010-0034-8

Key, R. M., Kozyr, A., Sabine, C. L., Lee, K., Wanninkhof, R., Bullister, J. L., et al. (2004). A global ocean carbon climatology: Results from Global Data Analysis Project (GLODAP). *Global Biogeochemical Cycles*, *18*, GB4031. https://doi.org/10.1029/2004GB002247

Khatiwala, S., Primeau, F., & Holzer, M. (2012). Ventilation of the deep ocean constrained with tracer observations and implications for radiocarbon estimates of ideal mean age. *Earth and Planetary Science Letters*, *325*, 116–125.

Kunze, E., Firing, E., Hummon, J. M., Chereskin, T. K., & Thurnherr, A. M. (2006). Global abyssal mixing inferred from lowered ADCP shear and CTD strain profiles. *Journal of Physical Oceanography*, *36*(8), 1553–1576.

Liang, X., Spall, M., & Wunsch, C. (2017). Global ocean vertical velocity from a dynamically consistent ocean state estimate. *Journal of Geophysical Research: Oceans*, *122*, 8208–8224. https://doi.org/10.1002/2017JC012985

Lisitsyn, A., Binns, R., Bogdanov, Y. A., Scott, S., Zonenshayn, L., Gordeyev, V., et al. (1991). Active hydrothermal activity at Franklin seamount, western Woodlark sea (Papua New Guinea). *International Geology Review*, *33*(9), 914–929.

Lumpkin, R., & Speer, K. (2007). Global ocean meridional overturning. *Journal of Physical Oceanography*, *37*(10), 2550–2562.

Lupton, J. (1998). Hydrothermal helium plumes in the Pacific Ocean. *Journal of Geophysical Research*, *103*(C8), 15,853–15,868.

Lupton, J. E., & Craig, H. (1981). A major helium-3 source at 15°S on the East Pacific Rise. *Science*, *214*(4516), 13–18.

Lupton, J. E., Pyle, D. G., Jenkins, W. J., Greene, R., & Evans, L. (2004). Evidence for an extensive hydrothermal plume in the Tonga-Fiji region of the South Pacific. *Geochemistry, Geophysics, Geosystems*, *5*, Q01003. https://doi.org/10.1029/2003GC000607

Macdonald, A. M., Mecking, S., Robbins, P., Toole, J., Johnson, G. C., Talley, L., et al. (2009). The WOCE-era 3-D Pacific Ocean circulation and heat budget. *Progress in Oceanography*, *82*(4), 281–325.

Matsumoto, K., Sarmiento, J. L., Key, R. M., Aumont, O., Bullister, J. L., Caldeira, K., et al. (2004). Evaluation of ocean carbon cycle models with data-based metrics. *Geophysical Research Letters*, *31*, L07303. https://doi.org/10.1029/2003GL018970

Mazloff, M. R., Heimbach, P., & Wunsch, C. (2010). An eddy-permitting Southern Ocean state estimate. *Journal of Physical Oceanography*, *40*(5), 880–899.

Munk, W. H. (1966). Abyssal recipes. *Deep Sea Research and Oceanographic Abstracts*, *13*(4), 707–730.

Nikurashin, M., & Ferrari, R. (2013). Overturning circulation driven by breaking internal waves in the deep ocean. *Geophysical Research Letters*, *40*, 3133–3137. https://doi.org/10.1002/grl.50542

Nocedal, J., & Wright, S. J. (2006). *Numerical optimization* (2nd ed.). New York: Springer.

Oeschger, H., Siegenthaler, U., Schotterer, U., & Gugelmann, A. (1975). A box diffusion model to study the carbon dioxide exchange in nature. *Tellus*, *27*(2), 168–192.

Olsen, A., Key, R. M., van Heuven, S., Lauvset, S. K., Velo, A., Lin, X., et al. (2016). The Global Ocean Data Analysis Project version 2 (GLODAPv2)—An internally consistent data product for the world ocean. *Earth System Science Data*, *8*(2), 297–323.

Orr, J. C., Najjar, R. G., Aumont, O., Bopp, L., Bullister, J. L., Danabasoglu, G., et al. (2017). Biogeochemical protocols and diagnostics for the CMIP6 Ocean Model Intercomparison Project (OMIP). *Geoscientific Model Development*, *10*(6), 2169–2199.

Pasquier, B., & Holzer, M. (2017). Inverse-model estimates of the ocean's coupled phosphorus, silicon, and iron cycles. *Biogeosciences*, *14*, 4125–4159.

Primeau, F. (2005). Characterizing transport between the surface mixed layer and the ocean interior with a forward and adjoint global ocean transport model. *Journal of Physical Oceanography*, *35*(4), 545–564.

Reid, J. L. (1997). On the total geostrophic circulation of the Pacific Ocean: flow patterns, tracers, and transports. *Progress in Oceanography*, *39*(4), 263–352.

Resing, J. A., Sedwick, P. N., German, C. R., Jenkins, W. J., Moffett, J. W., Sohst, B. M., & Tagliabue, A. (2015). Basin-scale transport of hydrothermal dissolved metals across the South Pacific Ocean. *Nature*, *523*(7559), 200.

Roshan, S., & DeVries, T. (2017). Efficient dissolved organic carbon production and export in the oligotrophic ocean. *Nature communications*, *8*(1), 2036.

Roshan, S., Wu, J., & Jenkins, W. J. (2016). Long-range transport of hydrothermal dissolved Zn in the tropical South Pacific. *Marine Chemistry*, *183*, 25–32.

Saito, M. A., Noble, A. E., Tagliabue, A., Goepfert, T. J., Lamborg, C. H., & Jenkins, W. J. (2013). Slow-spreading submarine ridges in the South Atlantic as a significant oceanic iron source. *Nature Geoscience*, *6*(9), 775–779.

Schlitzer, R. (2007). Assimilation of radiocarbon and chlorofluorocarbon data to constrain deep and bottom water transports in the world ocean. *Journal of Physical Oceanography*, *37*(2), 259–276.

Schlitzer, R. (2016). Quantifying He fluxes from the mantle using multi-tracer data assimilation. *Philosophical Transactions of the Royal Society A*, *374*(2081), 20150288.

Skinner, L. C., Primeau, F., Freeman, E., de la Fuente, M., Goodwin, P., Gottschalk, J., et al. (2017). Radiocarbon constraints on the glacial ocean circulation and its impact on atmospheric CO_2. *Nature Communications*, *8*(16), 010.

Sprintall, J., Wijffels, S. E., Molcard, R., & Jaya, I. (2009). Direct estimates of the Indonesian Throughflow entering the Indian Ocean: 2004–2006. *Journal of Geophysical Research*, *114*, C07001. https://doi.org/10.1029/2008JC005257

Srinivasan, A., Top, Z., Schlosser, P., Hohmann, R., Iskandarani, M., Olson, D. B., et al. (2004). Mantle 3He distribution and deep circulation in the Indian Ocean. *Journal of Geophysical Research*, *109*, C06012. https://doi.org/10.1029/2003JC002028

Stark, S., Jenkins, W. J., & Doney, S. C. (2004). Deposition and recirculation of tritium in the North Pacific Ocean. *Journal of Geophysical Research*, *109*, C06009. https://doi.org/10.1029/2003JC002150

Stommel, H. (1982). Is the South Pacific helium-3 plume dynamically active? *Earth and Planetary Science Letters*, *61*(1), 63–67.

Tagliabue, A., Bopp, L., Dutay, J.-C., Bowie, A. R., Chever, F., Jean-Baptiste, P., et al. (2010). Hydrothermal contribution to the oceanic dissolved iron inventory. *Nature Geoscience*, *3*(4), 252.

Talley, L. D. (2003). Shallow, intermediate, and deep overturning components of the global heat budget. *Journal of Physical oceanography*, *33*(3), 530–560.

Thacker, W. C., & Long, R. B. (1988). Fitting dynamics to data. *Journal of Geophysical Research*, *93*(C2), 1227–1240.

Top, Z., Eismont, W., & Clarke, W. (1987). Helium isotope effect and solubility of helium and neon in distilled water and seawater. *Deep Sea Research Part A Oceanographic Research Papers*, *34*(7), 1139–1148.

Tschumi, T., Joos, F., Gehlen, M., & Heinze, C. (2010). Deep ocean ventilation, carbon isotopes, marine sedimentation and the deglacial co2 rise. *Climate of the Past*, *6*(5), 1895–1958.

Tsujino, H., Hasumi, H., & Suginohara, N. (2000). Deep Pacific circulation controlled by vertical diffusivity at the lower thermocline depths. *Journal of Physical Oceanography*, *30*(11), 2853–2865.

Vranes, K., Gordon, A. L., & Ffield, A. (2002). The heat transport of the Indonesian Throughflow and implications for the Indian Ocean heat budget. *Deep Sea Research Part II: Topical Studies in Oceanography*, *49*(7), 1391–1410.

Wanninkhof, R. (1992). Relationship between wind speed and gas exchange over the ocean. *Journal of Geophysical Research*, *97*(C5), 7373–7382.

Wanninkhof, R., Park, G.-H., Takahashi, T., Sweeney, C., Feely, R., Nojiri, Y., et al. (2013). Global ocean carbon uptake: Magnitude, variability and trends. *Biogeosciences*, *10*(3), 1983–2000.

Warner, M., & Weiss, R. (1985). Solubilities of chlorofluorocarbons 11 and 12 in water and seawater. *Deep Sea Research Part A Oceanographic Research Papers*, *32*(12), 1485–1497.

Weber, T., John, S., Tagliabue, A., & DeVries, T. (2018). Biological uptake and reversible scavenging of zinc in the global ocean. *Science*, *361*(6397), 72–76.

Weiss, R. F. (1971). Solubility of helium and neon in water and seawater. *Journal of Chemical & Engineering Data*, *16*(2), 235–241.

Well, R., Lupton, J., & Roether, W. (2001). Crustal helium in deep Pacific waters. *Journal of Geophysical Research*, *106*(C7), 14,165–14,177.

Well, R., Roether, W., & Stevens, D. P. (2003). An additional deep-water mass in Drake Passage as revealed by 3He data. *Deep Sea Research Part I: Oceanographic Research Papers*, *50*(9), 1079–1098.